Purely Leptonic Decays of Heavy Flavour Mesons

Tome Antičić

A thesis submitted to

The Johns Hopkins University

in conformity with the requirements for the degree of
Doctor of Philosophy

Baltimore, Maryland
1997

Abstract

Using the data sample of 1,475,000 $Z \to q\overline{q}(\gamma)$ events collected during 1994 runs with the L3 detector at LEP, we have searched for purely leptonic decays of heavy flavour mesons $D_s^- \to \tau^- \overline{\nu}_\tau$ and $B^- \to \tau^- \overline{\nu}_\tau$. The analysis technique is based on the identification of τ-decay products in the hadronic jets and on the reconstruction of the energy and direction of heavy mesons using kinematic constraints. A clear signal for the $D_s^- \to \tau^- \overline{\nu}_\tau$ decays is observed in the invariant mass distribution $M_{\gamma D_s^-}$ corresponding to the decay chain $D_s^{*-} \to \gamma D_s^-$, $D_s^- \to \tau^- \overline{\nu}_\tau$. The branching fraction for $D_s^- \to \tau^- \overline{\nu}_\tau$ decays is measured to be $\mathcal{B}(D_s^- \to \tau^- \overline{\nu}_\tau) = (\, 7.4 \pm 2.8(\text{stat}) \pm 1.6(\text{syst}) \pm 1.8(\text{norm})\,)\,\%$. No indication for the $B^- \to \tau^- \overline{\nu}_\tau$ decays is observed in the data. The upper limit on the branching fraction $\mathcal{B}(B^- \to \tau^- \overline{\nu}_\tau) < 5.7 \times 10^{-4}$ is set at 90% CL.

Thesis Advisor: Professor Chih-Yung Chien

Contents

List of Figures

List of Tables

If I had eight hours to cut down a tree,
I'd spend seven sharpening my axe.

Attributed to Abraham Lincoln

Acknowledgements

Doing my graduate work at the L3 experiment at LEP as part of the Johns Hopkins group has been one of the most exciting and rewarding times of my life. I am very grateful to all the people who made this possible.

In particular, special thanks go to my advisor Professor Chih-Yung Chien, whose support and patience at all stages of my work was invaluable, and who could see the light at the end of the tunnel even when things seemed very murky to me indeed. Further thanks go to Peter Fisher who first got me to CERN and introduced me to garlic steaks and forced me to learn ZEBRA, a painful but invaluable skill. I also owe my gratitude to Professor Aihud Pevsner who started me in high energy experimental physics, and was always ready to help out if any problem arose.

It would have been impossible to do my work without Andrei Kunin, who patiently guided me through all the steps of my analysis, and was at hand whenever I got stuck at some seemingly insurmountable problem. Andreas Gougas was great company in the office we shared, and I am very grateful for the many interesting discussions I had with him and for the support he gave me, both physics related and otherwise.

I would like to thank Tom Paul and Lucas Taylor who helped me out in many intricacies concerning L3 and its software, and whose input in my thesis is very appreciated. Special thanks go to Suen Hou, with whom I learned many things about silicon sensors and analysis techniques.

I have to thank the other members of the Hopkins High Energy group, notably Barry Blumenfeld and Bruce Barnett for their unselfish help and encouragement. The same goes for my fellow graduate students (now Doctors) from Hopkins at L3, James Gerald and Doris Kim.

Joe Orndorff, Dave Newman and Jack Spangler taught me invaluable skills about engineering and professionalism, for which I'll always be grateful to them.

Thanks also go to the rest of my exam board commitee, namely Jon Bagger, Werner Love, and Steven Zucker.

And last, but not least, I would like to thank my father, mother, and my siblings Zvonimir, Marija, and Hrvoje for their unqualified support in my endeavor. Its success would not have been possible without them.

Chapter 1

Theory and Motivation

An overview of the current understanding of particle physics is presented in this chapter, with emphasis on the relevant physics for the analysis.

1.1 Standard Model

The current view of the fundamental building blocks of nature is based on the existence of two types of pointlike elementary particles: fermions and bosons. Fermions carry halfinteger spin and thus form antisymmetric states under the exchange of identical particles while bosons have integer spin and hence obey Bose-Einstein statistics. All matter is composed of fermions, while the role of bosons is to mediate forces between the fermions. The fermions are further subdivided into quarks and leptons, grouped into three families of two. Thus the leptons consist of the electron, the muon, the tau, and their corresponding neutrinos, while the quarks are the up and down quark, the charm and strange quark, and the top and bottom quark.

There are four types of forces in nature: the strong, the weak, the electromagnetic and the gravitational force. The strength of the latter is too small to influence, at present, any measurements in particle physics. The remaining three are mediated by gluons, the $W^{\pm}$ and Z bosons, and the photon, respectively. The neutrinos only feel the weak interaction, while the charged leptons (e, μ, τ) also feel the electromagnetic interaction. The quarks participate in all three of the particle forces.

The Standard Model incorporates the theories of quantum chromodynamic-

s(gluon exchange)(QCD), quantum electrodynamics (photon exchange)(QED), and the weak theory($W^{\pm}$, Z boson exchange). It is based on a Lagrangian with a locally gauge invariant $SU(3)_C \otimes SU(2)_L \otimes U(1)_Y$ symmetry. The $SU(3)_C$ corresponds to the QCD theory [1], while the $SU(2)_L \otimes U(1)_Y$ part unifies the electromagnetic and weak forces [2]. The latter is referred to as the Standard Model of Electroweak interactions.

The $SU(2)_L$ is a doublet consisting of a left–handed charged lepton and a left-handed neutrino, while $U(1)_Y$ is a right–handed charged lepton. The requirement of gauge invariance prevents the Lagrangian from providing mass to the charged leptons or to the gauge bosons. The addition of a complex doublet scalar field(the Higgs field) to the overall Lagrangian and then the application of the so-called spontaneous symmetry breaking mechanism enables masses to be added to the bosons while preserving gauge invariance at the same time. In this mechanism the Higgs field acquires a non-zero vacuum expectation value. This results in masses given to the vector bosons $W^{\pm}$ and Z by using 3 degrees of freedom from the Higgs doublet. The one remaining degree of freedom results in a real boson, the Higgs boson, which to date has not been found yet. The Higgs mechanism also generates masses for the charged fermions. Tables 1.1 and 1.2 show the main properties of the fermions and bosons, respectively.

Leptons			Q	I	I_3
$\begin{pmatrix} \nu_e \\ e \end{pmatrix}_L$	$\begin{pmatrix} \nu_\mu \\ \mu \end{pmatrix}_L$	$\begin{pmatrix} \nu_\tau \\ \tau \end{pmatrix}_L$	0	1/2	+1/2
			−1	1/2	−1/2
e_R	μ_R	τ_R	−1	0	0
Quarks			Q	I	I_3
$\begin{pmatrix} u \\ d' \end{pmatrix}_L$	$\begin{pmatrix} c \\ s' \end{pmatrix}_L$	$\begin{pmatrix} t \\ b' \end{pmatrix}_L$	+2/3	1/2	+1/2
			−1/3	1/2	−1/2
u_R	c_R	t_R	+2/3	0	0
$d_R{}'$	$s_R{}'$	$b_R{}'$	−1/3	0	0

Table 1.1: Quantum numbers for fermions in the Standard Model. The primes on the quarks are to indicate that the mass eigenstates do not correspond to the electroweak eigenstates. Q is the charge, I is the weak isospin, and I_3 is the third component of the isospin.

Boson	Charge	Mass	Spin
γ	0	0 GeV	1
Z	0	91.2 GeV	1
$W^{\pm}$	± 1	80.2 GeV	1
H	0	> 70 GeV	0

Table 1.2: Quantum numbers for bosons in the Standard Electroweak Model.

An important property of quarks is that they, unlike leptons, can also decay between families, albeit with much smaller amplitudes than transitions within the same doublet. As a result the mass eigenstates do not correspond to the electroweak eigenstates. Thus the electroweak eigenstates are expressed as shown in equation 1.1. The 3×3 matrix is known as the CKM matrix. By convention the up, charm, and top quarks are left as they are, while it is the down, strange, and bottom quarks which get rotated.

$$\begin{pmatrix} d' \\ s' \\ b' \end{pmatrix} = \begin{pmatrix} V_{ud} & V_{us} & V_{ub} \\ V_{cd} & V_{cs} & V_{cb} \\ V_{td} & V_{ts} & V_{tb} \end{pmatrix} \begin{pmatrix} d \\ s \\ b \end{pmatrix} \tag{1.1}$$

For example, the decay $b \rightarrow u^{+}l^{-}\bar{\nu}$ is proportional to V_{ub}. Knowledge of these numbers is crucial in calculating any process involving charged quark currents.

In the Feynman diagram formalism fermions and bosons are connected by interaction vertices, as shown in Figure 1.1. In these expressions e is the unit of electric charge and $\gamma_i (i = 1, 2, ..., 5)$ are the Dirac gamma matrices. The vector and axial vector coupling constants v_f and a_f are defined by:

$$v_f = I_3^f - 2Q_f \sin^2\theta_W \qquad \text{and} \qquad a_f = I_3^f \tag{1.2}$$

where I_3^f indicates the weak isospin third component, and Q_f the electric charge in units of e of the fermion under consideration. The angle θ_W is the weak mixing angle defined in terms of the $W^{\pm}$ and Z masses as:

$$\sin^2\theta_W = 1 - \frac{M_W^2}{M_Z^2} \tag{1.3}$$

The mixing angle $\sin^2\theta_W = 0.2312$ together with the Fermi constant $G_F = 1.6639 \times 10^{-5}$ GeV^{-2} and the fine structure constant $\alpha = 1/137.036$ constitute the

set of free parameters in the Standard Model (not counting the Higgs mass and the fermion masses and mixings). They are related by the expression

$$G_F = \frac{\pi\alpha}{\sqrt{2}M_W^2 \sin^2\theta_W} \tag{1.4}$$

In this case the value of α is at the Z mass and not rest, and is equal to $\alpha = 1/128.27$.

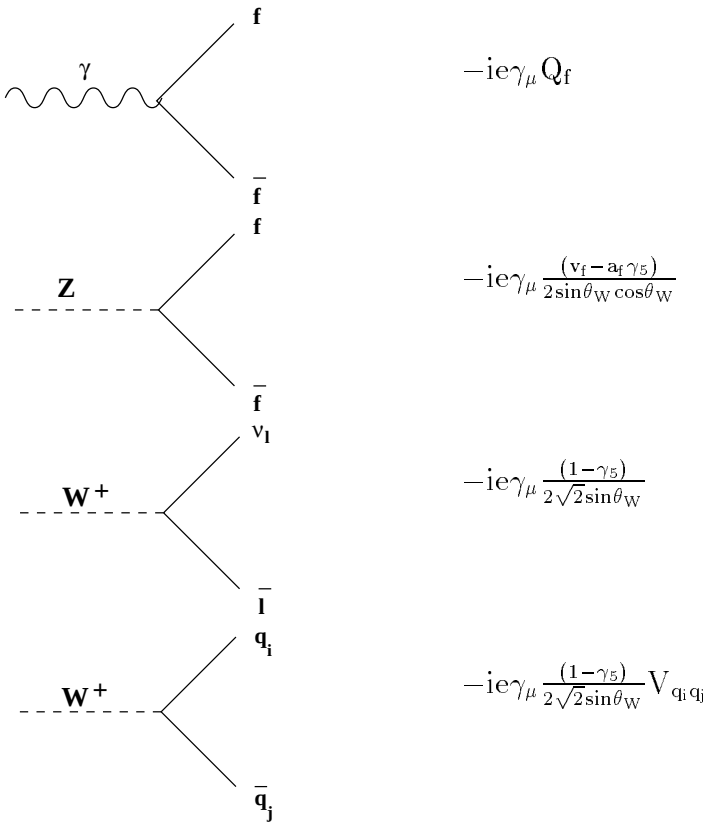

Figure 1.1: The electroweak couplings within the framework of the Standard Model.

1.2 Quark pair production

An electron and a positron can annihilate into a photon or a Z boson. For low centre of mass energies $\sqrt{s}$ the process $e^+e^- \rightarrow q\bar{q}$ will be dominated by single photon exchange. With increasing energies the Z exchange comes into play and when energies in the vicinity of the Z resonance at $\sqrt{s} \approx 92$ GeV are reached, the Z exchange dominates the process. Figure 1.2 shows the two lowest order Feynman diagrams. The contribution to the process from the Higgs channel $e^+e^- \rightarrow H^\circ \rightarrow q\bar{q}$ is neglected.

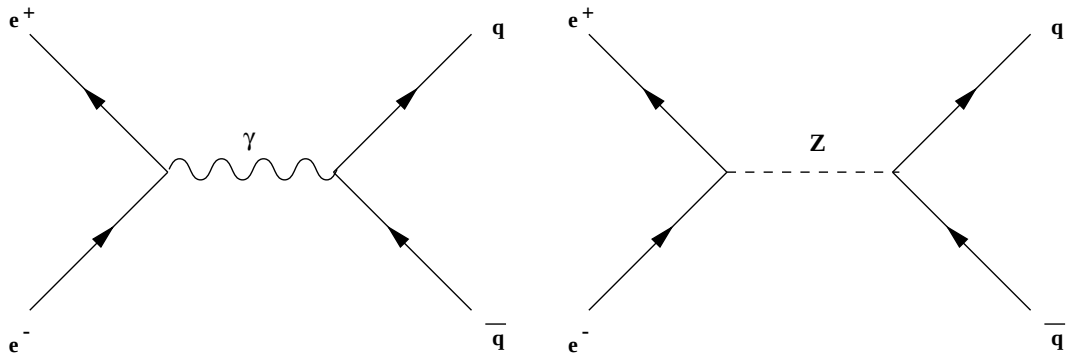

Figure 1.2: The Feynman diagrams for the reaction $e^+e^- \rightarrow q\bar{q}$ in lowest order.

On the assumption that the masses of both the incoming particles and the final state quarks can be ignored, the lowest order differential cross-section can then be written as:

$$\frac{d\sigma_0(s)}{d\Omega} = \frac{3\alpha^2}{4s}\left\{G_1(s)(1+\cos^2\theta) + 2G_3(s)\cos\theta\right\} \tag{1.5}$$

with θ the polar angle between the incoming electron and outgoing quark, and G_1 and G_3

$$G_1(s) = Q_q^2 - 2\chi_1^2 v_e v_q Q_q Re\chi_0(s) + \chi_1^4(v_e^2+a_e^2)(v_q^2+a_q^2)\left|\chi_0(s)\right|^2 \tag{1.6}$$

$$G_3(s) = -2\chi_1^2 a_e a_q Q_q Re\chi_0(s) + 4\chi_1^4 v_e a_e v_q a_q \left|\chi_0(s)\right|^2 \tag{1.7}$$

with

$$\chi_0(s) = \frac{s}{s - M_Z^2 + iM_Z\Gamma_Z} \qquad \text{and} \qquad \chi_1 = \frac{1}{2\sin\theta_W\cos\theta_W} \tag{1.8}$$

The symbol Γ_Z refers to the total Z decay width, which equals the inverse of the Z lifetime; i.e. $\Gamma_Z = 1/\tau_Z$. The total Z decay width is the sum of the partial widths of all the possible decay channels of the Z:

$$\Gamma_Z = \sum_f \Gamma_f \tag{1.9}$$

In expression 1.5, which is also called the Born approximation of the cross section, three types of terms can be distinguished. The terms which are proportional to $|\chi_0(s)|^2$ correspond to the exchange of the Z. As the Z exchange dominates the process, these terms are the most significant ones and are responsible for the Breit-Wigner shape of the cross section, with a maximum at $s = M_Z^2\,(1 + \Gamma_Z^2/M_Z^2)^2$. The terms proportional to $Re\chi_0(s)$ are due to the (γ, Z) interference, while the remaining term is the γ exchange contribution. At the Z resonance both these effects are very small compared to the Z exchange contribution.

Higher order corrections to the diagrams of Figure 1.2 are needed to determine the full reaction rates. These are:

- QED Corrections, which consist of real or virtual photons added to the Born level diagrams. Examples are initial and final state radiation, virtual photon loops or interference between final and initial state radiation.
- Weak Corrections, which are one-loop diagrams not covered by the QED effects, and contain corrections to the (γ, Z) propagators, vertex corrections (with virtual photon contributions excluded) and box diagrams with two massive boson exchanges.
- QCD Corrections, which involve final state gluon radiation.

The QED corrections are the most important contribution to the tree level Born approximation, with the QCD and weak effects relatively small. The initial state photon radiation yields by far the largest correction to the cross section. This shifts the Z peak cross section to a higher energy, and reduces it by approximately 35%. The final state QED correction is the result of final state photon interference with the lowest order Z decay process. It changes the cross section by a factor:

$$1 + \delta_{QED} = 1 + \frac{3\alpha Q_f^2}{4\pi} \tag{1.10}$$

and is therefore small: only 0.019% for the quarks with charge $\frac{1}{3}$ (d,s,b) and 0.077% for those with charge $\frac{2}{3}$ (u,c,t).

The most important weak corrections are propagator corrections and initial and final state vertex correction terms (see Figure 1.3). The weak corrections can be taken into account by keeping the Born cross section formula but redefining the Standard Model parameters it contains. The resulting expression is called the "improved" Born approximation of the cross section. The parameters in this improved expression are called effective and are distinguished from the original parameters by a bar above the symbol. These redefined Standard Model parameters can be written as follows for the $Z^0 \to b\bar{b}$ case:

$$\bar{a}_f = I_3^f + \frac{2}{3}\delta_{fb}\Delta_\rho + ... \quad (1.11)$$

$$\bar{v}_f = (I_3^f - 2Q_f \sin^2\bar{\theta}_W) + \frac{2}{3}\delta_{fb}\Delta_\rho + ... \quad (1.12)$$

$$sin^2\bar{\theta}_W = \sin^2\theta_W + \cos^2\theta_W\Delta_\rho + \frac{\alpha}{4\pi}\left[\ln\left(\frac{M_H}{17.3}+1\right) - 2\right] + ... \quad (1.13)$$

$$G_F = G_F(1+\Delta_\rho) + ... \quad (1.14)$$

with

$$\Delta_\rho = \frac{3\sqrt{2}G_F m_t^2}{16\pi^2} \quad (1.15)$$

Here δ_{fb} is a Kronecker-δ, i.e. 1 for b quarks and 0 otherwise, and M_H is the Higgs mass expressed in GeV. Formulas 1.11 and 1.15 give the dominating terms of the weak corrections on the quantities a_f, v_f, $\sin^2\bar{\theta}_W$ and G_F. The suppressed (...) terms stand for the smaller order corrections.

The QCD corrections involve additional gluons in the tree level diagrams of Figure 1.2 and its higher order diagrams, the most important of which are shown in Figure 1.3. Unlike photons, the gluons do not couple to the leptons but only to the final state quarks. The main complication in calculating QCD effects is that the strong coupling constant α_s is much larger than the QED coupling constant. Also, the quark masses have to be taken into account. This results in a modification of the cross section by a factor of(up to order α_s):

$$1 + \delta_{QCD} = 1 + \frac{3\alpha_s}{\pi} \quad (1.16)$$

For heavy flavours these corrections induce a shift of 4 to 5% in the total cross section.

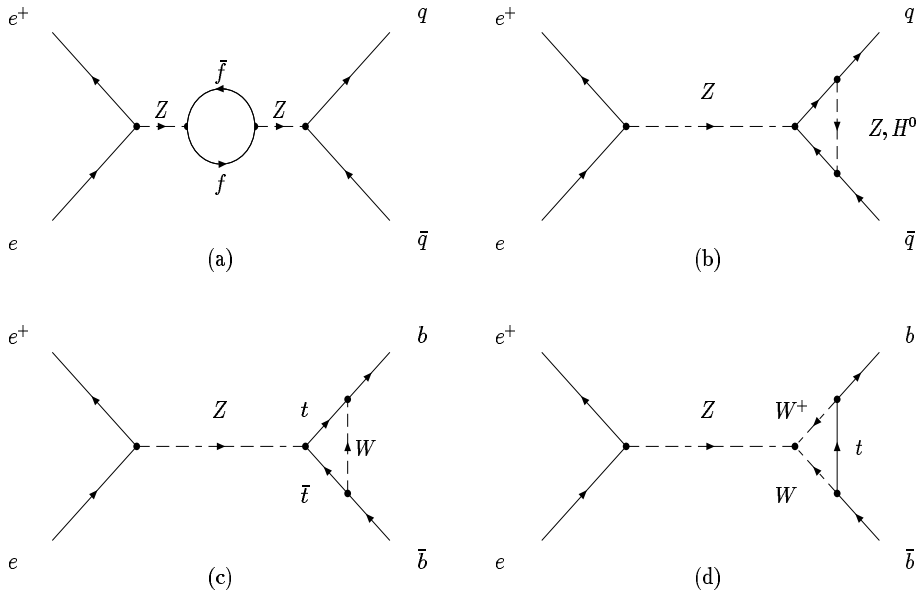

Figure 1.3: Feynman diagrams corresponding to a) a Z propagator correction, b) a final state vertex correction, resulting from the Z and the Higgs, and (c and d) from the W boson for the case of a $b\bar{b}$ quark final state.

Figure 1.4 shows the cross section for the process $Z^0 \to b\bar{b}$ in the Born approximation and in the improved Born approximation with all QED, weak, and QCD corrections included.

1.3 The Process $q\bar{q} \to$ hadrons

The Process $q\bar{q} \to$ hadrons is a complex one. From the original back-to-back $q\bar{q}$ pair usually only a rough di-jet structure remains. QCD is able to predict certain parts of this process, but the non-perturbative nature means that modeling is intensively used. There are four stages to this:

1. $Z^0 \to q\bar{q}$ pair creation. This is covered by the Standard Model electroweak theory, as explained in the previous sections.

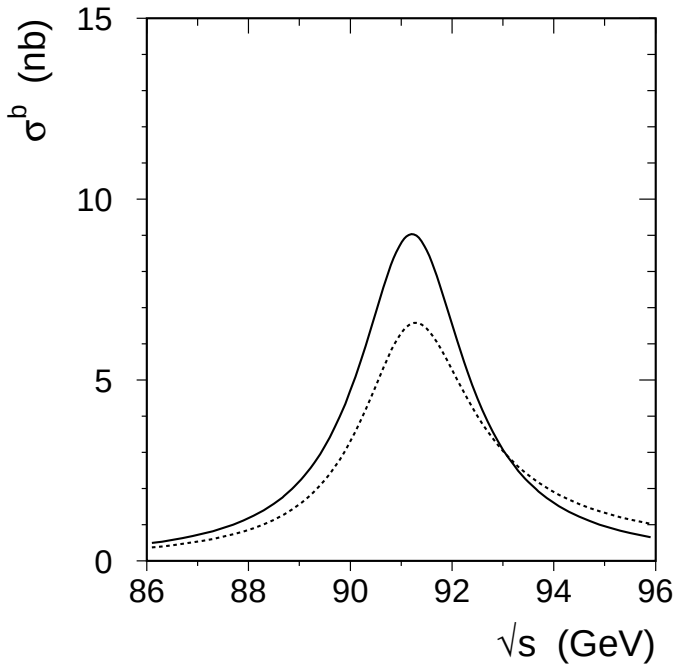

Figure 1.4: The energy dependence of the cross section in the Born approximation (solid line) and after applying all QED, weak, and QCD corrections (dashed line).

2. Parton radiation. The $q\bar{q}$ pair may radiate gluons. which in turn may radiate other partons. Perturbative QCD is used as part of *parton shower models* to model this stage.

3. Hadronisation. Here perturbative QCD cannot be used and instead the *string fragmentation* model is used. This describes hadronisation as a $q\bar{q}$ pair separating from each other with a coloured string attached between the quarks. The separating quarks stretch the string, whose tension is linear with respect to distance. At a certain tension the string breaks, forming a new $q\bar{q}$ pair. This continues until the string invariant mass falls below some energy level. Quantitatively, this is described using a fragmentation function, which is the

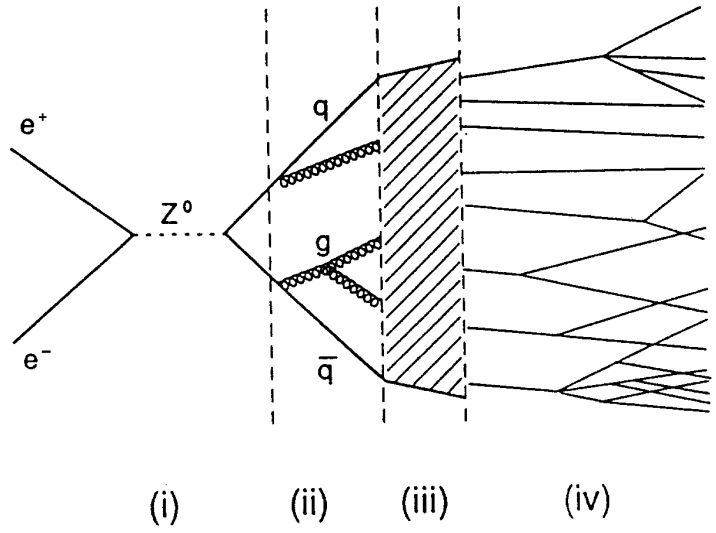

Figure 1.5: A schematic representation of the four stages of the Z decaying into a quark-antiquark pair subsequently fragmenting into a set of final state hadrons.

probability distribution of the z variable:

$$z = \frac{\left(E + p_{\parallel}\right)_{\text{hadron}}}{(E + p)_{\text{quark}}} \tag{1.17}$$

in which $(E + p)_{\text{quark}}$ is the sum of energy and momentum of the primary quark, and $\left(E + p_{\parallel}\right)_{\text{hadron}}$ the sum of the energy and the momentum component parallel to the direction of the leading fragmentation parton.

Two types of fragmentation function are employed, depending on the mass of the original quark. Light quarks fragment according to the Field-Feynman fragmentation function, while heavy quarks(c and b) fragment according to

the Peterson function [3]

$$f_{(z)} \propto \frac{1}{z}\left(1 - \frac{1}{z} - \frac{\epsilon_q}{1-z}\right)^{-2} \tag{1.18}$$

where ϵ_q is a function of the quark mass.

Usually the more intuitive parameter, the ratio of the primary hadron energy to the beam energy ,x_ϵ, is quoted. For b quarks, $\langle x_\epsilon\,(b)\rangle$ is around 0.71, while for c quarks $\langle x_\epsilon\,(c)\rangle$ is around 0.49. The b quark thus carries a relatively large percentage of the beam energy, making for more narrow and energetic jets.

4. Decays of hadrons. In the final stage of hadronisation, the short-lived hadrons decay into detectable particles. Phenomenological parameters such as lifetimes and branching ratios are used.

1.4 Purely leptonic decays

The hadrons from the $Z^0 \to q\bar{q} \to$ hadrons chain can decay in several modes: semileptonically, leptonically, or hadronically. The corresponding Feynman diagrams are shown in Figure 1.6.

Any decay is fully expressed in terms of two currents, sandwiching the appropriate boson. Leptonic decays, for example, would then result from the $W^\pm$ mediated interaction between a quark current and a leptonic current. The $W^\pm$ bosons result in transitions between an upper and a lower fermion of a doublet, giving so-called charged currents. The interaction Lagrangian involving charged currents coupled to the $W^\pm$ boson is shown in equation 1.19.

$$\mathcal{L}_{\text{int}} = -\frac{g}{\sqrt{2}}\left(\mathcal{J}^\mu W_\mu^+ + \mathcal{J}^{\mu\dagger} W_\mu^-\right) \tag{1.19}$$

where the charged current for quark transitions is

$$\mathcal{J}^\mu = \sum_{i,j} V_{i,j} J_{i,j}^\mu = \sum_{i,j} \bar{u}_i \gamma^\mu \frac{1}{2}\left(1 - \gamma_5\right) V_{i,j} d_j \tag{1.20}$$

The indices i and j run over all quark generations. The $\bar{u}_i$ are the field operators for the u, c, t quarks, and $\bar{d}_j$ are the field operators for the d, s, b quarks. The $V_{i,j}$ are the elements of the CKM matrix.

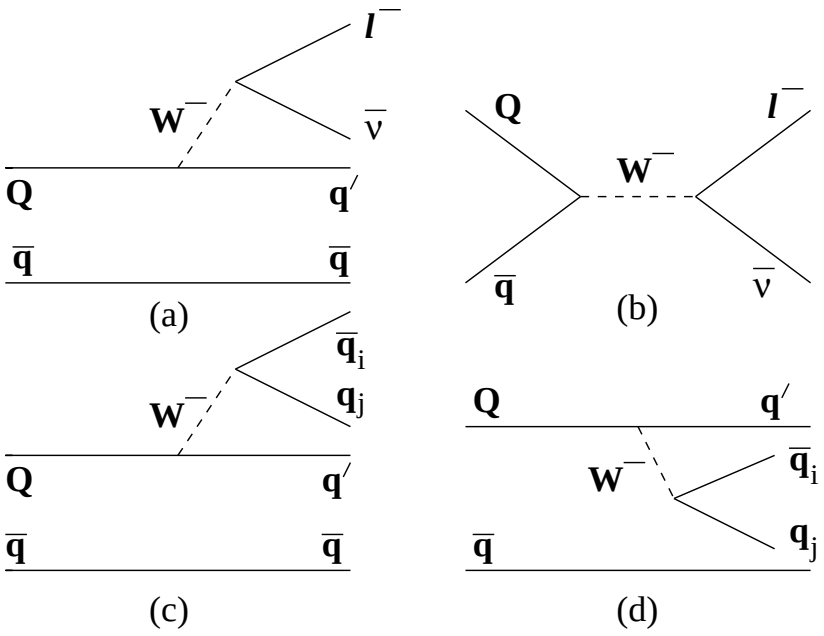

Figure 1.6: Lowest order representations for charged current decays of a meson: a)semileptonic decay, b)leptonic decay, c)hadronic decay, d) hadronic decay

For leptons the charged current is similar, but the analog to the CKM matrix is the unit matrix.

In practice the transition amplitudes involving hadronic currents cannot easily be calculated, as the quarks are always embedded in hadrons, and thus nonperturbative strong-interaction effects are involved.

For processes with energies much less than the $W^{\pm}$ mass, one can use an approximate form for the $W^{\pm}$ propagator, together with the relation $G_F/\sqrt{2} = g^2/(8M_W^2)$ to simplify equation 1.20. For purely leptonic decays of a pseudoscalar meson one then gets a simple expression for the amplitude

$$\mathcal{M}\left(M_{Q\bar{q}} \to l^{-}\bar{\nu}\right) = i\frac{G_F}{\sqrt{2}} V_{qQ} f_M L^{\mu} q_{\mu} \tag{1.21}$$

The q_μ is the four–momentum of the meson,while the f_M is the so-called meson decay constant, which measures the overlap of a quark and antiquark at zero separation. The L^μ is the leptonic current, and can be written in terms of the

Dirac spinors u_l and v_ν

$$L^\mu = \bar{u}_l \gamma^\mu (1 - \gamma_5) v_\nu \tag{1.22}$$

The corresponding decay width is

$$\Gamma(M_{Q\bar{q}} \to l^- \bar{\nu}) = \frac{G_F^2 \, f_M^2 \, |V_{qQ}|^2 \, M_l^2 \, M}{8\pi} \, (1 - \frac{M_l^2}{M^2})^2 \tag{1.23}$$

where M_l and M are the masses of the lepton and the charged meson $M_{Q\bar{q}}$, respectively.

1.4.1 Decay constants

The determination of the above mentioned decay constants is interesting as they play an important role in extracting physics quantities from diverse measurements. They give absolute normalisations of numerous heavy-flavour transitions, including mixing, semi-leptonic and non-leptonic decays. For example, the determination of the $B^0 - \bar{B}^0$ mixing ratio can be expressed as a function of the CKM parameters times f_B^2 [4]. A measurement of a purely leptonic decay branching ratio, unlike semileptonic or nonleptonic decays, is the most reliable way to extract the pseudoscalar decay constant, because it does not involve any QCD corrections.

In this analysis the method for extracting the decay constant f_{D_s} is described, among other measurements. There are three purely leptonic decay modes for the D_s^-: electronic, muonic and taonic. Due to helicity suppression (see Equation 1.23) the taonic mode $D_s^- \to \tau^- \overline{\nu}_\tau$ gives the largest branching ratio of the three, and thus is the mode analysed.

There are several competing theoretical approaches to calculate f_{D_s}, but due to the non–perturbative calculations they vary significantly in their predictions. In particular, theoretical models predict the value of f_{D_s} to be between 190–360 MeV [5–7]. Many models can more reliably predict the ratios $f_{D_s^-} : f_D : f_B$, where f_D and f_B are the decay constants for the charged D and B meson, respectively [8].

Measurements of the leptonic decays $D_s^- \to \mu^- \bar{\nu}_\mu$ have been reported by several experiments [9–11]. The only measurement to date for the $D_s^- \to \tau^- \overline{\nu}_\tau$ channel is by the BES collaboration [12] based on only two events. It thus suffers from a large uncertainty, giving a branching ratio of $\mathcal{B}(D_s^- \to \tau^- \overline{\nu}_\tau) = (12^{+20}_{-10})\%$. The branching fraction $\mathcal{B}(D_s^- \to \tau^- \overline{\nu}_\tau)$ is expected to be $0.0485 \times (f_{D_s}/250 \text{ MeV})^2$ according to equation 1.23. The theoretical value of around 200 for f_{D_s} indicates that the $D_s^- \to \tau^- \overline{\nu}_\tau$ channel may be accessible at the LEP collider in Geneva.

Similarly, the decay constant f_B can be extracted from purely leptonic decay of the B meson. The theoretical predictions vary in the range of 120–230 MeV [13]. The expected branching fraction for $\mathcal{B}(B^- \to \tau^- \overline{\nu}_\tau)$ is around 0.5×10^{-4} for $f_B = 190$ MeV and $|V_{ub}| = 0.003$. This is a very difficult number to access. So far only limits have been set [14] [15], with the best published one at 1.8×10^{-3} [14]. However, certain supersymmetric models predict a possible large enhancement of this decay, as is explained in the next section.

1.5 Type II Higgs models

Even though there is no definite experimental data contradicting the Standard Model, there is wide agreement that it is incomplete as it has a very large number of arbitrary parameters. Also, loop diagrams contributing to the Higgs propagator diverge at high energies. Further, there is the unnatural distinction between fermions and bosons. One would expect that a truly fundamental theory should not have these problems.

This has led to several more complete theories being proposed which address these and other drawbacks of the Standard Model. Some of the most promising ones are the "Supersymmetric Theories". In supersymmetry every fermion(quarks and leptons) has a supersymmetric spin zero partner (squarks and sleptons). At the same time every boson($W^\pm$,Z, Higgs, photon, gluon) has a spin $\frac{1}{2}$ partner. The presence of the supersymmetric partners in loop corrections cancel out the divergences in the Higgs propagator. Hence from a theoretical view the Supersymmetric theories successfully deal with the previously mentioned problems.

At least two Higgs doublets are required, as opposed to one in the Standard Model. These doublets separately give masses to up-type quarks and to down-type quarks and charged leptons. In this case we have the so-called "Minimal Supersymmetric Model"(MSSM), where five extra physical bosons arise(in addition to the photon,$W^\pm$ and Z). Among these are two charged scalar bosons $H^\pm$.

One can extend the Standard Model to also contain two Higgs doublets as opposed to one. The case where one Higgs doublet couples to d-type quarks and charged leptons, while the other one couples to u-type quarks are called Type II Higgs doublet models. As explained above,the MSSM models also fall under this classification.

There is no evidence to date for any of these supersymmetric particles. Instead, only limits have been set for their masses. In particular, the $B^- \to \tau^- \overline{\nu}_\tau$ decays

enable the possible determination of the mass of the charged Higgs for Type II Higgs doublet models [16], as the branching ratio $\mathcal{B}(B^- \to \tau^- \overline{\nu}_\tau)$ is enhanced by a factor of

$$\left[\left(\frac{m_B}{M_{H^\pm}}\right)^2 \tan^2_\beta - 1\right]^2 \tag{1.24}$$

with $\tan\beta$, the ratio of the vacuum expectation values of the charged Higgs bosons.

Hence the measurement of the branching ratio $\mathcal{B}(B^- \to \tau^- \overline{\nu}_\tau)$ could constrain type II Higgs doublet models, in addition to a possible determination of the decay constant f_B.

Chapter 2

The L3 Detector

In this chapter an overview of the Large Electron Positron collider(LEP) is given, followed by a more detailed description of the L3 detector [17] which collected the data used for the physics analysis described in this thesis.

2.1 The LEP e^+e^- storage ring

The LEP storage ring is currently the largest particle accelerator in the world. It is designed to provide colliding e^+e^- beams with centre-of-mass energies up to 200 GeV at a design luminosity of $\mathcal{L} = 10^{31}\mathrm{cm}^{-2}\mathrm{s}^{-1}$. Until the end of 1995 the machine was running at the Z resonance region.

LEP is built in a tunnel of 26.7 km circumference and passes through both Swiss and French territory. As illustrated in Figure 2.1, the ring has eight bending and eight straight sections of 2840 m and 490 m length respectively. The four LEP experiments ALEPH, DELPHI, L3 and OPAL are located in alternating straight sections. Superconducting quadrapole magnets are placed on both sides of the experiments to compress the beams in the vertical direction for increased luminosity. Turning around the LEP ring, electrons and positrons of 45 GeV radiate 117 MeV of synchrotron radiation per turn. This is compensated by the 128 16 MW radio-frequency accelerating cavities installed along the beam path.

Beams are created by a series of accelerating, storing, and transfer processes. Positrons are created by colliding an electron beam, accelerated by a linear accelerator up to 200 MeV, on a tungsten target. A second linear accelerator is used to accelerate these positrons to an energy of 600 MeV, after which they are injected

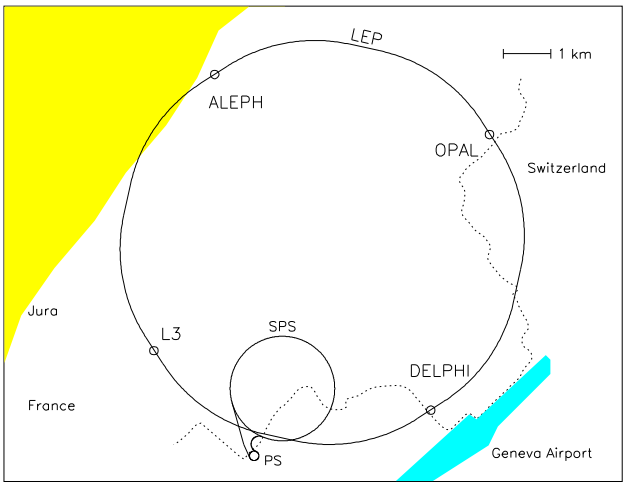

Figure 2.1: LEP geography.

in an Electron-Positron Accumulator ring(EPA). The electrons are directly accelerated by the 600 MeV accelerator and then also placed in the EPA. Next, both electrons and positrons are passed on to the Proton Synchrotron(PS) and accelerated to 3.5 GeV. This is followed by a transfer to the Super Proton Synchrotron (SPS) where the particles are boosted to an energy of 20 GeV. At this stage the electrons and positrons are injected in either four or eight bunches into LEP. The beams are then ramped to collision energies.

The data sample for the 1994 running period consists of a total integrated luminosity of 64 pb^{-1}, collected at the Z peak.

2.2 The L3 detector

The L3 detector design emphasises high resolution energy measurements of electrons, photons, muons, and jets produced in e^+e^- collisions at energies up to 200 GeV. A perspective view of the L3 is shown in Figure 2.2. Figure 2.3 and Figure 2.4 show $r-\phi$ and $r-z$ slices respectively.

Going from closest to furthest away from the interaction point, the following

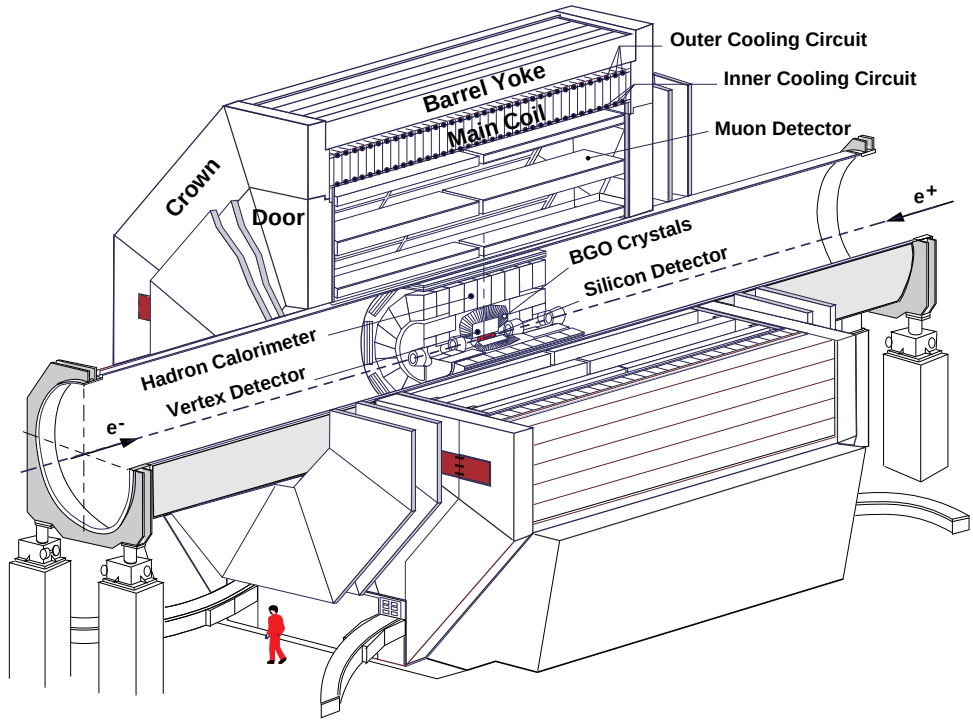

Figure 2.2: Perspective view of L3.

subdetectors comprise L3:

- A high precision silicon vertex detector
- A central tracking detector
- An electromagnetic calorimeter
- Scintillation counters for trigger information
- A hadron calorimeter
- Muon chambers
- A solenoid magnet

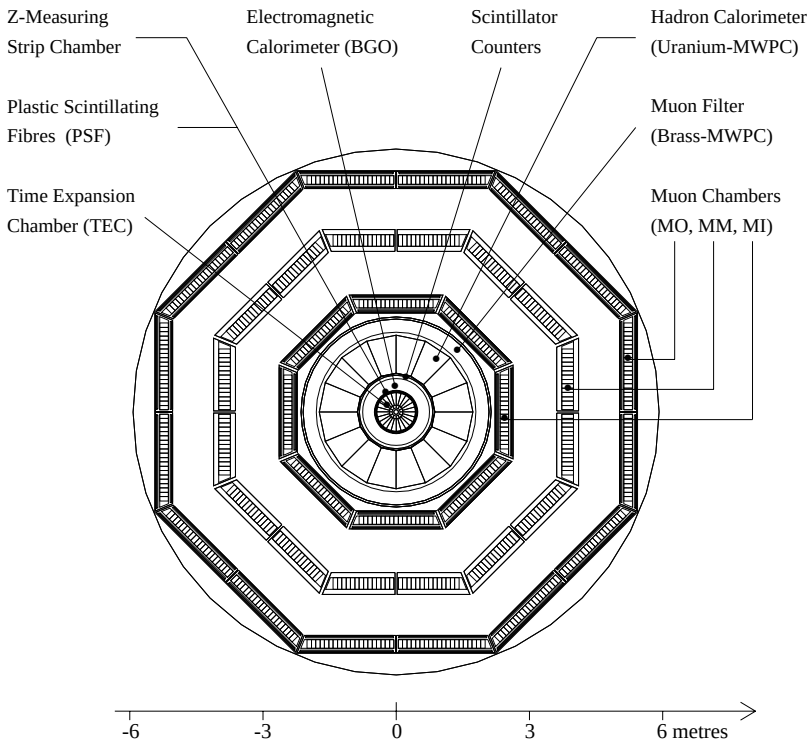

Figure 2.3: $r - \phi$ view of L3.

In addition, there is a monitor to determine the luminosity of the e^+e^- beam.

All the subdetectors are installed in a conventional magnet providing a uniform field of 0.5 T along the beam axis. The calorimeters, scintillators, luminosity monitors and the central tracker are mounted within a 32 m long, 4.45 m diameter iron support tube concentric with the beam line. Three layers of driftchambers forming the muon spectrometer surround this tube. This global setup was chosen to optimise the muon momentum resolution, since the transverse momentum resolution is proportional to Bl^2, with B the magnetic field and l the track length.

Spherical coordinates describe positions and directions, with the z-axis defined by the e^- beam (Figure 2.4). The origin is taken as the e^+e^- collision point.

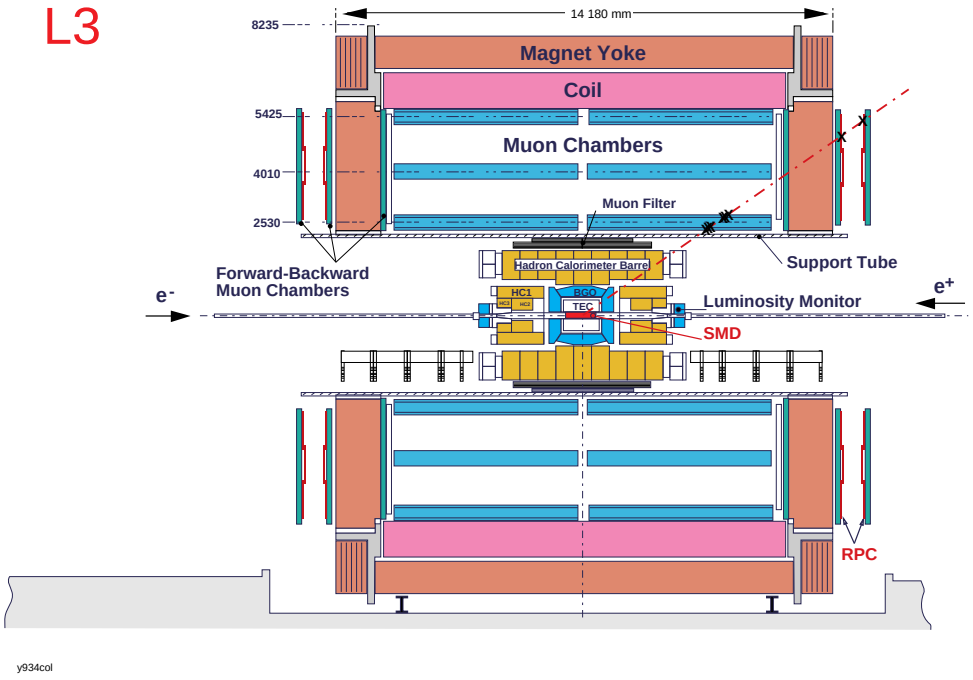

Figure 2.4: $r-z$ view of L3.

2.2.1 Magnet

The magnet consists of an octagonal coil made of welded aluminum plates and a soft iron return yoke. The coil has an inner radius of $\approx$ 5.9 m and a length of $\approx$ 12 m. The coil carries a current of 30 kA and generates a field of 0.5 T with variations of $\leq$1% within the magnet volume.

2.2.2 Muon Spectrometer

The muon chamber system consists of sixteen octants arranged into two octagonal ferris wheels. Each octant (Figures 2.5) consists of five drift chambers: two in the outer layer, two in the middle layer, and one in the inner layer. These "P-chambers" measure the $r-\phi$ track coordinate, and the inner and outer layers also contain "Z-chambers" which measure the $z-$coordinate.

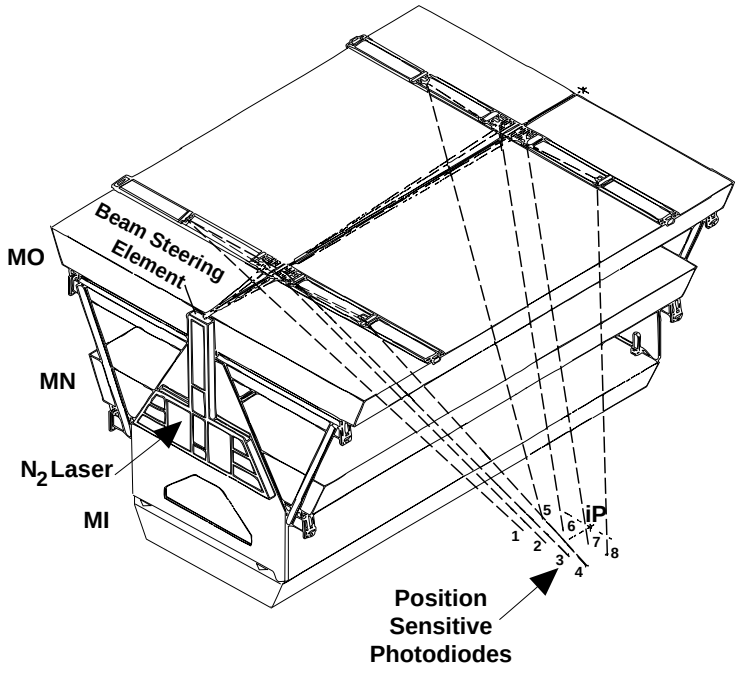

Figure 2.5: A muon spectrometer octant.

The design goal for the muon chamber system was to measure the momentum of 45 GeV charged particles with a resolution of $\sigma_P/P \approx 2.5\%$. The combined momentum measuring lever arm for a track passing through all three layers is 2.9 m, resulting in a sagitta of s = 3.7 mm for a 45 GeV charged particle. In order to achieve the design resolution, chamber alignment tolerances must be maintained to better than 30 μm, and $r-\phi$ coordinate measurements in each layer must approach a precision of ≈ 50 μm.

2.2.3 Hadron Calorimeter

The hadron calorimeter(HCAL) measures the energies of hadrons traversing it via total absorption. It can also identify muons, as these leave a minimum ionising signature.

The HCAL consists of a barrel and two endcaps covering the angular regions

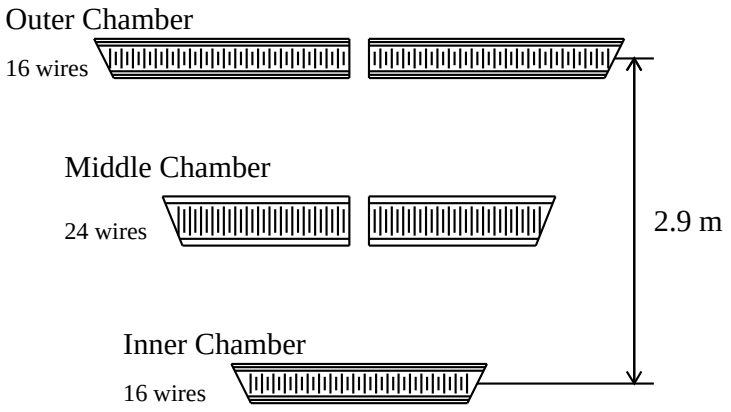

Figure 2.6: Front view of a muon spectrometer octant. The Z-chambers are located on either surface of the inner and outer P-chambers.

of $|\cos\theta| < 0.82$ and $0.82 < |\cos\theta| < 0.995$ respectively. Both barrel and endcaps cover the whole azimuthal range; thus a coverage of 99.5% of 4π is achieved.

The barrel hadron calorimeter consists of 9 rings of 16 modules each (see Figure 2.7). Its length is 4.7 m and it has an outer radius of 1.8 m. The endcaps consist of one outer and two inner rings. Each of these rings is split into two removable half-rings, thus allowing access to the inner detectors. The HCAL modules of both barrel and endcap are made of 5.5 mm thick layers of depleted uranium plates interspersed with proportional wire chambers. Uranium was chosen as the absorbing material due to the need for a compact calorimeter to allow the largest possible lever arm for the muon spectrometer. As a result, between six and seven nuclear absorption lengths are achieved. In order to further reduce punchthrough from hadronic debris into the muon system, the inner wall of the support tube is lined with a brass muon filter, adding an additional one absorption length to the hadron calorimeter. The wires are oriented along and perpendicular to the z-axis, enabling three dimensional cluster determination. The wires are grouped in towers for readout purposes, leading to a typical spatial segmentation of $\delta\theta = \delta\phi = 2°$.

The calorimeter system allows determination of the jet axis with a resolution of about 2.5° and charged pion energy measurement with resolution better than

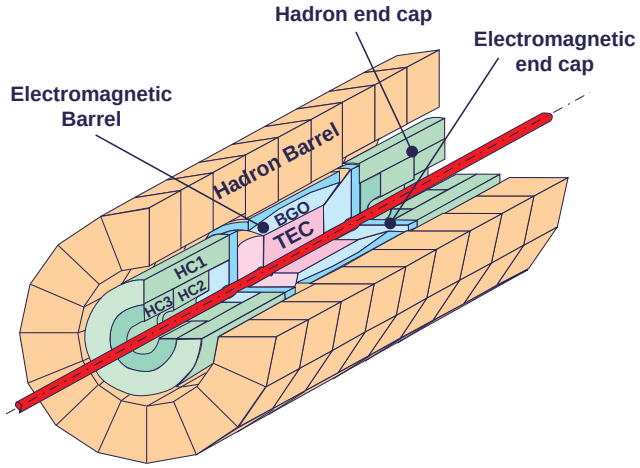

Figure 2.7: The hadron calorimeter.

20% above about 15 GeV.

2.2.4 Scintillation Counters

The scintillation counters are positioned between the hadron and electromagnetic calorimeters, as shown in Figure 2.8. It consists of thirty plastic scintillating counters read out by photomultiplier tubes.

Its main purpose is the rejection of cosmic muons, as these can mimic dimuon events if they pass close to the interaction vertex. However, e^+e^- interactions strike opposing scintillators simultaneously, while cosmics need about 6 ns to achieve this. The good time resolution of 0.5 ns enables rejection of these cases.

2.2.5 Electromagnetic Calorimeter

The electromagnetic calorimeter [18](ECAL) is positioned between the time expansion chamber and the hadron calorimeter. It is made out of a total of 10752 Bismuth Germanate (BGO) crystals arranged in a barrel and two endcap regions.

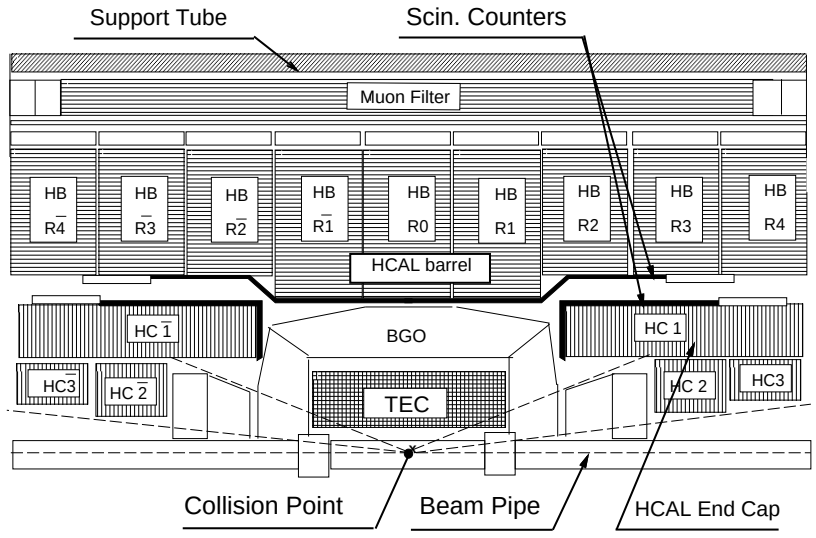

Figure 2.8: A slice of L3 showing the location of, among other things, the scintillator system.

The barrel regions covers a polar angular range of $-0.72 < \cos\theta < 0.72$ and the endcaps extend the coverage down to $0.80 < |\cos\theta| < 0.98$. Each crystal has the shape of a truncated pyramid arranged so that they all point towards the interaction region, as shown in Figure 2.9. The dimensions of a single crystal are shown in Figure 2.10. The area of the inner surface is $\approx 2 \times 2$ cm^2 and the length is 24 cm. This corresponds to about 1 nuclear interaction and 22 radiation lengths.

The BGO has excellent energy and spatial resolution for photons and electrons over a wide energy range between 100 MeV and 100 GeV. At 100 MeV the energy resolution is about 5%, while between 1 GeV and 100 GeV the resolution is better than 2%. Due to the fine segmentation of the crystal relative to the BGO Molière radius(2.3 cm), electromagnetic showers typically extend over an array of 3×3 crystals, allowing precise reconstruction of shower centroids. The spatial resolution for incident electrons has been measured to be 4 mm at 1 GeV, down to 1 mm at 45 GeV. With an average distance between the crystal front faces and

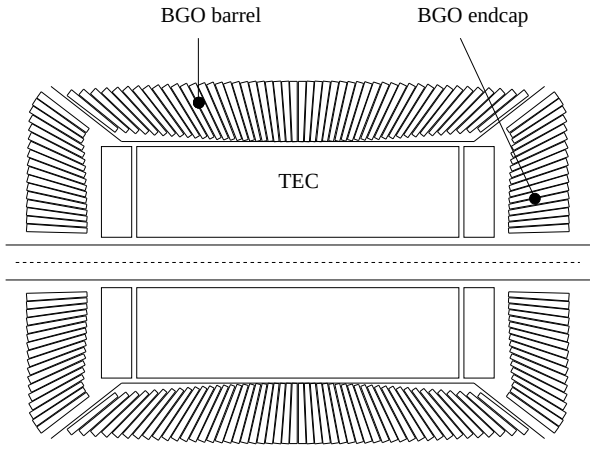

Figure 2.9: $r - z$ view of the electromagnetic calorimeter (BGO) showing the projective geometry.

the interaction point of 60 cm, this position resolution translates into an angular resolution of 4 mrad to 7 mrad. The fine segmentation also makes the BGO very efficient at discriminating electrons from pions with a rejection ratio of $\approx 1000 : 1$.

2.2.6 Central Tracking Chamber

The L3 central tracking chamber consists of the Time Expansion Chamber(TEC), the Z-detector, the Silicon Micro Vertex Detector(SMD), and the Forward Tracking Chamber(FTC).

The main component of the central tracking chamber is the TEC, which measures the $r - \phi$ coordinate. The size constraints imposed by the electromagnetic calorimeter result in a relatively small lever arm for TEC of 31.7 cm. When this is combined with only a 0.5 T field, a single hit resolution of 50 μm is needed to identify the charge of a 50 GeV particle at the 95% confidence level. These tight constraints lead to the use of the time expansion principle for the central tracker [19]. In this design a high field amplification region is separated from a low field drift region by two planes of grounded drift wires, as shown in Figure 2.11. The uniform electric field within the drift region results in a linear drift-time to

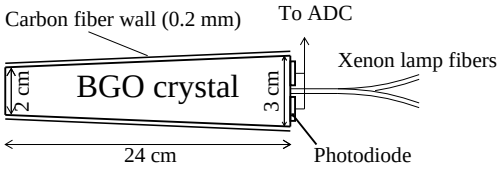

Figure 2.10: A single BGO crystal.

drift-distance relationship of around 6 μm/ns.

TEC consists of 12 inner and 24 outer sectors with all wires mounted in the z-direction (Figure 2.12). The inner sectors each have 8 while the outer have 54 sense or anode wires, giving a maximum of 62 sampled track points. A plane of cathode wires separates the sectors. Figure 2.13 shows a detailed view of one inner and two outer sectors.

A resolution of $\sigma \approx 60$ μm for the inner, and $\sigma \approx 50$ μm for the outer sector is achieved when a centre-of-gravity technique is used to determine the drift time. The average resulting transverse momentum resolution is $\sigma_{(1/P_T)} \approx 0.018$ GeV^{-1} for tracks with $|\cos\theta| < 0.72$ (barrel region).

Precise measurements of the z-coordinate for charged tracks are made with the Z-detector surrounding the TEC. It is made of two cylindrical multiwire proportional chambers employing cathode strip readout. The strips are tilted with respect to the $z-$axis by 69° and 90° for the inner chamber, and by $-69°$ and $-90°$ for the outer chamber. The resulting $z-$coordinate resolution is about 320 μm. The FTC gives additional points for tracks in the forward/backward region. It consists of drift chambers placed between the TEC endflanges and the BGO endcaps.

The Silicon Micro Vertex Detector [20] is located between the beampipe and the TEC, and increases the lever arm of the TEC by 4.8 cm. It is made of two cylindrical layers, placed at 6 and 8 cm from the interaction region. Each contains 12 ladders which consist of 4 double-sided 300 μm thick silicon sensors. The readout strips on the outer sides of each ladder are along the $z-$axis (and thus read out the $r-\phi$ coordinate) with a pitch of 50 μm. The strips on the inner side are transverse to the beam direction (and thus read out the z coordinate) with a pitch of 150/200 μm on the central/forward region of the $z-$side. In total, about 73000 readout channels are built into the detector, covering a polar angle range down to 22°. The resolution is 10 μm at the $r-\phi$ face, and 25 μm at the z

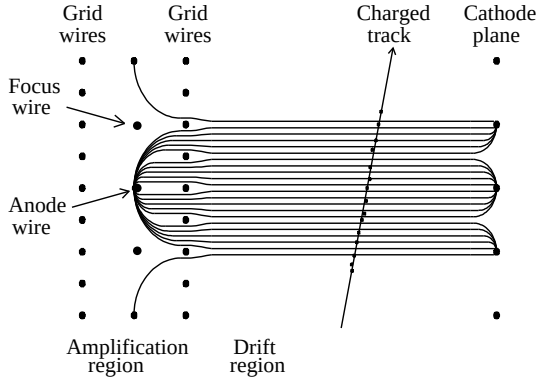

Figure 2.11: Amplification and drift regions in the TEC.

face. As a result the track momentum and direction determination are significantly improved.

2.2.7 Luminosity Monitor

The luminosity monitor measures the LEP beam luminosity in the L3 detector. The time integrated luminosity is given by N_{BB}/σ_{BB}, where N_{BB} is the number of accepted Bhabha events and σ_{BB} is the Bhabha cross section. This cross section is very large at low angles and is dominated by $t-$channel photon exchange, a well understood QED process.

The luminosity detector consists of a BGO electromagnetic calorimeter, proportional wire chambers, and Silicon Luminosity Monitors(SLUM's) positioned at 2.7 m on either side of the interaction point. These provide a luminosity measurement precise to 0.16%.

2.2.8 Online Trigger System

The LEP beam crossing period is 11 μs in 8×8 mode. About 100 ms is required to fully digitise all L3 subdetector signals and write an event to tape. The L3 trigger

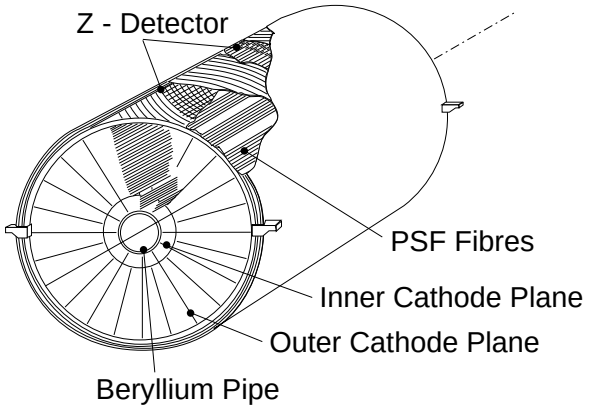

Figure 2.12: Perspective view of the TEC, Z-chamber, and PSF.

system performs a rapid analysis of the response of the various subdetectors at each beam crossing in order to determine whether a candidate e^+e^- event was produced. The goal is to minimise dead time that results from writing information from crossings with no detected particles, or from background events due to, for example, beam-gas interactions or cosmic rays. The trigger system is divided into three levels of increasing complexity. Each of the three levels applies several selection criteria which are logically OR'ed to produce a trigger.

Level-1 Trigger

Level-1 is based on five separate triggers; these come from the calorimetry, the luminosity monitor, the scintillation counters, the muon chambers, and the TEC. A positive result from any of the five causes the fine digitisation to commence for analysis by the subsequent levels. Level-1 produces a typical trigger rate of less than 8 Hz.

Calorimeter Trigger: This trigger is designed to select events which deposit energy in the electromagnetic or hadronic calorimeters, such as $e^+e^-, \tau^+\tau^-$, hadronic events, and $\nu\bar{\nu}\gamma$. The inputs consist of the analog sums of groups of BGO crystals and hadron calorimeter towers; barrel and endcap BGO crystals are grouped into $32\phi \times 16\theta$ blocks and hadron calorimeter towers are grouped into

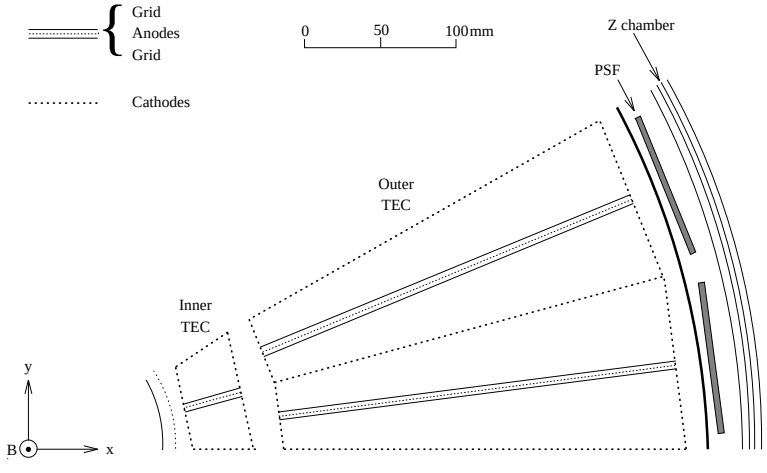

Figure 2.13: Geometry of a TEC sector.

16×11 blocks for layers less than about one absorption length and 16×13 blocks for deeper layers. The event is accepted if the BGO energy exceeds 25 GeV in the barrel and endcaps or 8 GeV in the barrel alone, or the total calorimetric energy exceeds 25 GeV in the barrel and endcaps or 15 GeV in the barrel alone. The $\theta - \phi$ projections are also used to search for clusters. The cluster threshold is 6 GeV, or 2.5 GeV for clusters in spatial coincidence with a track from the TEC trigger. The main source of background for this trigger is electronic noise, and the trigger rate is typically 1 to 2 Hz.

Scintillator Trigger: The scintillator system is used in level-1 to trigger on high multiplicity events. Events with at least 5 hits spread over 90° are selected. The trigger rate is typically 0.1 Hz. This trigger is practically background free.

Muon Trigger: The muon trigger selects events with at least one penetrating charged particle. Events are selected if hits in the muon chambers can be formed into a track with transverse momentum greater than 1 GeV. At least 2 P-layers and 3 Z-layers are required. Cosmic muons are rejected by requiring one good scintillator hit within 15 ns of the beam crossing. A 1 Hz trigger rate is typical.

Luminosity Trigger: Signal processing for this trigger is similar to that for the calorimeter trigger. An event is selected if any of the following criteria are met: two back-to-back depositions with $\geq$ 15 GeV, total energy on one side $\geq$ 25 GeV and on the other $\geq$ 5 GeV, or total energy on either side $\geq$ 30 GeV. A typical

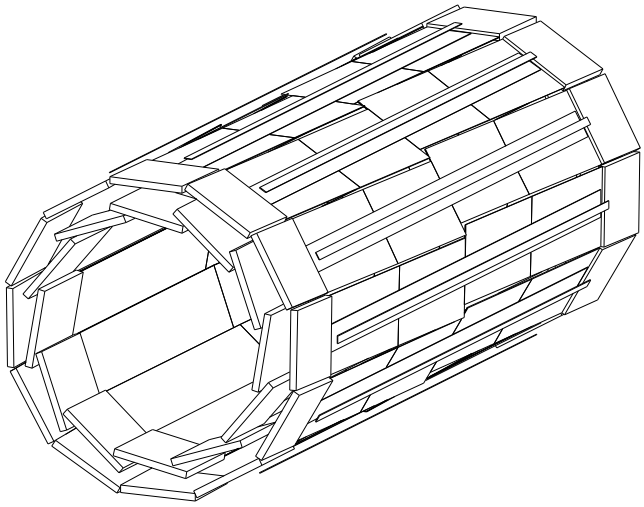

Figure 2.14: A perspective view of the SMD

trigger rate is 1.5 Hz for normal beam conditions.

TEC Trigger: The TEC trigger selects events with charged tracks. Tracks are required to have a transverse momentum of more than 150 MeV, and an event is selected if at least two tracks are found with acolinearity less than 60°. The TEC trigger rate is generally around 1 Hz, but can increase by several Hz during bad beam conditions.

Level-2 Trigger

Level-2 attempts to reject background events selected by level-1. At this level, more time can be spent analysing an event without incurring additional deadtime, and furthermore signals from different subdetectors can be correlated. Level-2 is effective in removing calorimeter triggers due to electronic noise, and TEC triggers due to beam-gas and beam-wall interactions. Events that produce more than one level-1 trigger are not rejected by level-2. The trigger rate after level-2 is typically less than 6 Hz.

Level-3 Trigger

This level executes a more detailed analysis of events that pass the previous two levels. Results of the fine digitizations are used, so more precise thresholds can be set for the calorimetry, which further reduces electronic noise. Muon triggers are required to fall within more stringent 10 ns scintillator coincidence, thereby reducing background from cosmic muons. Tracks selected by the TEC trigger are correlated with at least 100 MeV of energy in the calorimeters and are checked for quality and for a common vertex. Events that produce more than one level-1 trigger are not rejected by level-3. After Level-3, the overall trigger rate is generally around 3 Hz. From analysis of TEC and energy trigger coincidences, the trigger efficiency for $e^+e^- \to Z \to q\bar{q}$ is found to exceed 99.9% [21].

2.3 Resolution

2.3.1 TEC resolution

A charged particle passing through the central tracker ionises the gas and the resulting free electrons drift to the anode wires. The drift time is translated into distance from the anode. From this the curvature and hence the momentum of the track is arrived at. Since the determined distance is normally distributed around its true position, so then is the measured sagitta. As the sagitta is inversely proportional to the transverse momentum, it is useful to quote TEC resolution in this way. Note that since the resolution of the sagitta is virtually independent on the curvature, then $\sigma_{(1/P_T)}$ is also independent of momentum.

To determine the resolution of TEC, an independent and accurate momentum determination is needed. Dimuon events fulfill this criteria as the accuracy of the muon chamber results in very little charge confusion, and the muon energy is very well determined.

The full track parameters consist of the TEC hits, SMD hits, and the fill vertex. A plot of the resulting resolution is shown in figure 2.15. In the plot four cases are plotted:

- Only TEC hits included in the track
- TEC and fill vertex included
- TEC and SMD hits are included

- TEC, SMD and fill vertex are included.

As can be seen, SMD substantially improves the resolution due to TEC alone. The resolution is strongly dependent on the azimuthal angle ϕ. This is due to particles passing close to the amplification region and to the cathodes which have nonuniform and high electric fields. In the drift region the resolution on the transverse momentum is found to be $\sigma_{(1/P_T)} \approx 0.018$ GeV^{-1}.

The momentum scale of TEC is also determined using dimuon events, again taking advantage of the good energy determination of the muons. The average shift in the TEC momentum scale turns out to be about 1.3%.

2.3.2 BGO resolution

The BGO is used for accurately determining the photon and electron energies. These properties are very important for the analysis, so a good knowledge of the energy scale and resolution is crucial.

$Z \rightarrow e^+e^-$ events were used to determine the energy scale at 45 GeV to be about 0.1%. For lower energies the π^0 invariant mass is used. At 1 GeV this accuracy is about 1%. The BGO energy resolution for photons and electrons is shown in Figure 2.19.

Further, hadrons also leave an energy deposition in the BGO. Accuracy of the hadronic energy scale is about 1.5%, determined from the position of the ρ invariant mass peak as shown in Figure 2.16. Data from the hadronic calorimeter was combined with the BGO for this measurement.

2.3.3 HCAL resolution

The HCAL energy resolution for charged pions is determined from testbeam data to be $\sigma_{E_{\pi^\pm}} \approx 55\%/\sqrt{E_{\pi^\pm}} + 8\%$.

For high pion energies, this gives a higher accuracy than the central tracker. For energies below about 15 GeV, TEC is more accurate. The procedure for combining the calorimetric energy measurement with the momentum measurement from TEC consists of maximizing the probability, P_{combined}, that the two measurements arise from the same underlying energy, ϵ:

$$P_{\text{combined}} = P(E_C; \epsilon, \sigma_C(\epsilon)) P(1/P_T; \epsilon, \sigma_{(1/P_T)}) \tag{2.1}$$

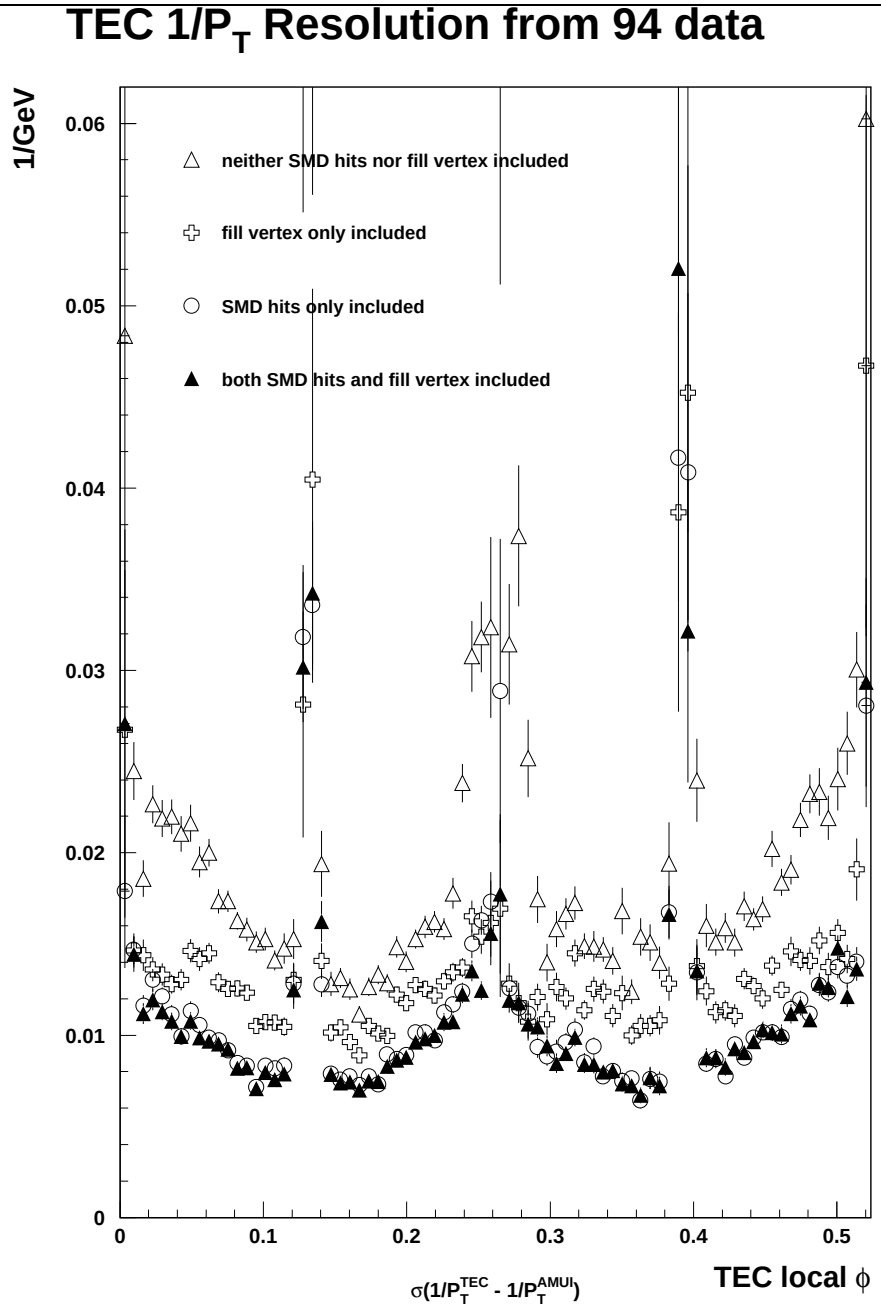

Figure 2.15: TEC momentum resolution versus TEC ϕ

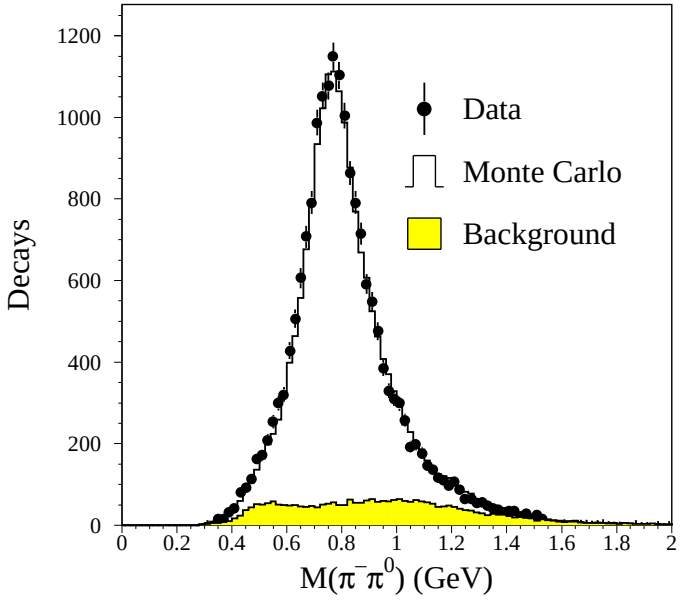

Figure 2.16: Invariant mass of the $\pi^-\pi^0$ system for selected $\tau^- \to \rho^-\nu_\tau$ decays

$$= \frac{1}{\sqrt{2\pi}\sigma_C^2(\epsilon)} \exp\left(-\frac{(E_C-\epsilon)^2}{2\sigma_C^2(\epsilon)}\right) \frac{1}{\sqrt{2\pi}\sigma^2_{(1/P_T)}} \exp\left(-\frac{(1/P_T - 1/\epsilon\sin\theta)^2}{2\sigma^2_{(1/P_T)}}\right)$$

where E_C is the measured energy in the calorimeters, $1/P_T$ is the inverse transverse momentum measured by the TEC, and $\sigma_C(\epsilon)$ and $\sigma_{(1/P_T)}$ are the errors on these quantities.

The Calorimetry, TEC, and combined resolutions for pions are shown in figure 2.17.

2.4 Muon Spectrometer resolution

The muon chamber resolution at high energies was determined using $Z \to \mu^+\mu^-$ events. Due to chamber inefficiencies and limited acceptance, not all tracks form hits in all three layers of the detector. For muons that produce hits in all three layers ("triplets"), the momentum is determined from the track sagitta. For the cases in which only two hits are formed ("doublets"), the momentum is computed from the difference of slopes in the two layers. The resolution for doublets is considerably worse than for triplets, as shown in Figure 2.18. The resolution is

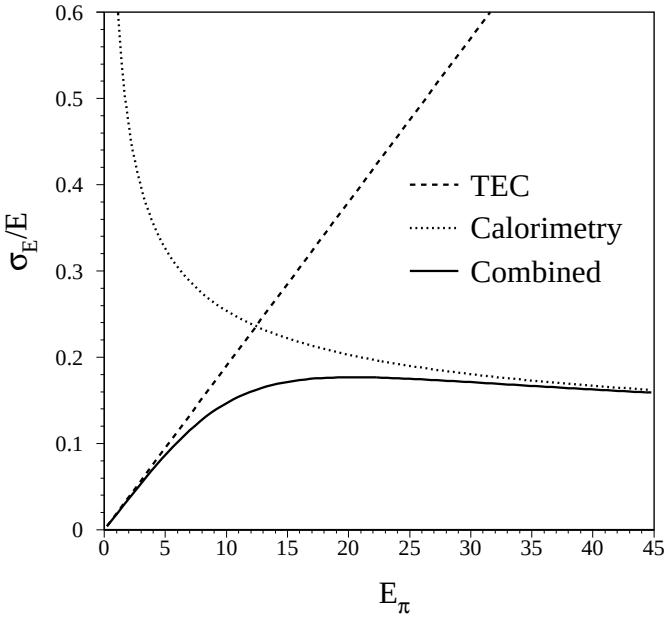

Figure 2.17: The resolution attained for charged pion energy measurement by combining measurements from the TEC and the calorimetry.

extrapolated to low energies using Monte Carlo to simulate the effects of multiple scattering in the calorimeters.

The accuracy of the muon momentum scale is estimated to be 0.2% at 45 GeV from a study of $Z \to \mu^+\mu^-$ decays, for which the muon energy is known from the beam energy.

A comparison of final resolutions for electrons, photons,muons, and charged pions is shown in figure 2.19.

2.5 Event reconstruction

The off-line event reconstruction follows several steps. First the information from the online data acquisition system is read and decoded. Next, reconstruction is carried out for each subdetector. Finally, associations are made between the reconstructed objects in different subdetectors to produce the kinematic variables that characterise an event.

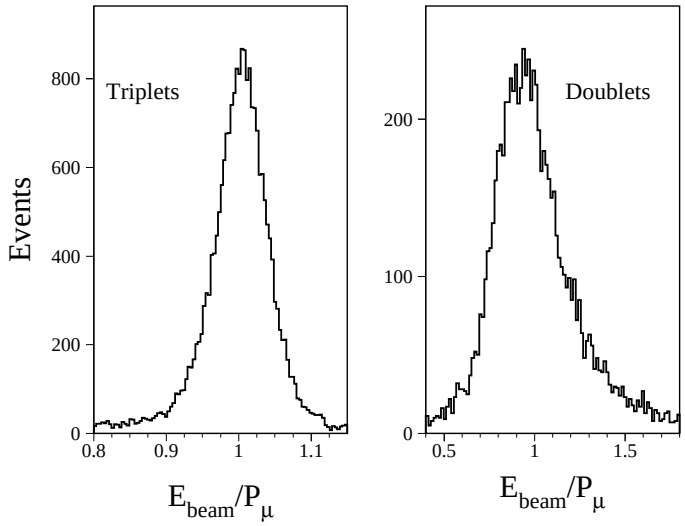

Figure 2.18: Muon chamber resolution for doublet and triplet tracks at $P_\mu \approx 45$ GeV from a sample of $Z \rightarrow \mu^+\mu^-$ events. The resolution is about 2.5% for triplets and 20% for doublets. Note the scale difference on the two plots.

Reconstruction is performed for all data written to tape, and reconstructed events are stored in several formats. The Master Data Reconstructed stream (MDRE) is produced from the procedure described below; it contains all the information necessary to repeat the full detector reconstruction. The typical size of an event in MDRE format is about 150 kBytes, compared to about 370 kBytes required for the raw data. Compressed data formats include the Data Summary Unit (DSU), which contains enough information for partial reconstruction of some detector objects. A DSU event typically occupies 22 kBytes.

2.5.1 Global reconstruction

Due to the fine segmentation of the calorimeters, it is possible to construct "Smallest Resolvable Clusters" (SRC's), each of which roughly corresponds to a single final state particle. Initially, tracks in the muon spectrometer are associated with clusters in the hadron calorimeter, bumps in the electromagnetic calorimeter, and tracks in the TEC. Remaining bumps in the electromagnetic calorimeter and clusters in the hadron calorimeter are then used to construct SRC's. The 3-momentum

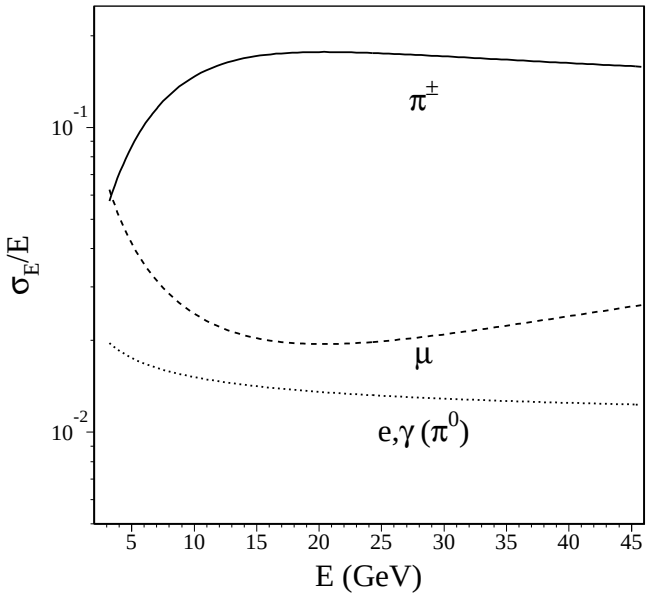

Figure 2.19: Resolutions as a function of energy for electrons, photons, muons, and charged pions.

for each SRC is then computed, where the total energy determines the magnitude and the energy weighted average of the positions of SRC components determines the direction. At this stage, an approximate energy calibration is used. During a second reconstruction pass, SRC's of identified particles can be computed using a more accurate calibration that depends on particle type.

SRC's and muons are used to compute a thrust axis, $\hat{T}$, for each event. The thrust axis is defined as the vector that minimises the expression,

$$\left| \sum_i \vec{P}_i \cdot \hat{T} \right| \tag{2.2}$$

where $\vec{P}_i$ is the momentum of the i'th particle.

2.6 Detector simulation

A precision measurement requires detailed understanding of detector response to the process under study. Computer simulation plays an important role in analysing the detector response and estimating backgrounds and systematic errors.

The Monte Carlo event simulation proceeds in three steps. First, an event generator simulates the physics process of interest, and produces a sample of final state particles and their 4-momenta. The simulated events are then propagated through a detailed representation of the L3 detector, which includes simulation of all the tracking and showering in the detector materials, as well as simulation of the response of active regions of the detector. The resulting digitised simulated events are then fed to the offline reconstruction program described above.

In this analysis the data collected in the vicinity of Z pole in 1994 are used. The integrated luminosity is 49.6pb corresponding to a sample of 1,475,000 $Z \to q\overline{q}(\gamma)$ events. For background study 3,261,500 $e^+e^- \to Z^0(\gamma) \to q\bar{q}$ decays with all q-flavours, according to the measured fractions, are generated using the JETSET 7.3 Monte Carlo generator [22]. For the efficiency studies 2500 events $D_s^- \to \tau^-\overline{\nu}_\tau$ followed by $\tau^- \to l^-\overline{\nu}_l\nu_\tau$ decays and 1500 $B^- \to \tau^-\overline{\nu}_\tau$ are generated. The Monte Carlo events are fully simulated in the L3 detector using the GEANT 3.15 program [23], which takes into account the effects of energy loss, multiple scattering and showering in the materials. The GHEISHA program [24] is used to simulate hadronic interactions in the detector materials.

Chapter 3

Particle Identification

3.1 Particle identification

The channels searched in the analysis are $D_s^- \to \tau^- \overline{\nu}_\tau$ and $B^- \to \tau^- \overline{\nu}_\tau$ decays. The goal is to separate these from the background. Reliable identification of particles in a hadronic enviroment are necesary for this, as described in this section. It is based upon the energy distribution in the electromagnetic and hadron calorimeters with respect to the trajectory of the charged track [25].

3.1.1 Electromagnetic and hadronic showers in the BGO

A photon and an electron leave a distinct electromagnetic signature in the BGO. It consists of a very narrow and symmetric shower, centered around the TEC track. More than 90% of the energy falls within a 3×3 crystal matrix around the maximum. Usually no energy gets deposited in the HCAL behind. Pions, on the other hand, have wide, asymetric showers. They also deposit a large amount of energy in the HCAL. Figure 3.1 shows typical electron and pion candidates.

An electromagnetic χ^2 is found to determine the nature of the shower profile. This measures how close the observed profile is with the expected one for an electromagnetic shower. Bhabha events were used to find the shower shape for electrons. Further testbeam studies showed the shape to vary very little for energies above 1 GeV.

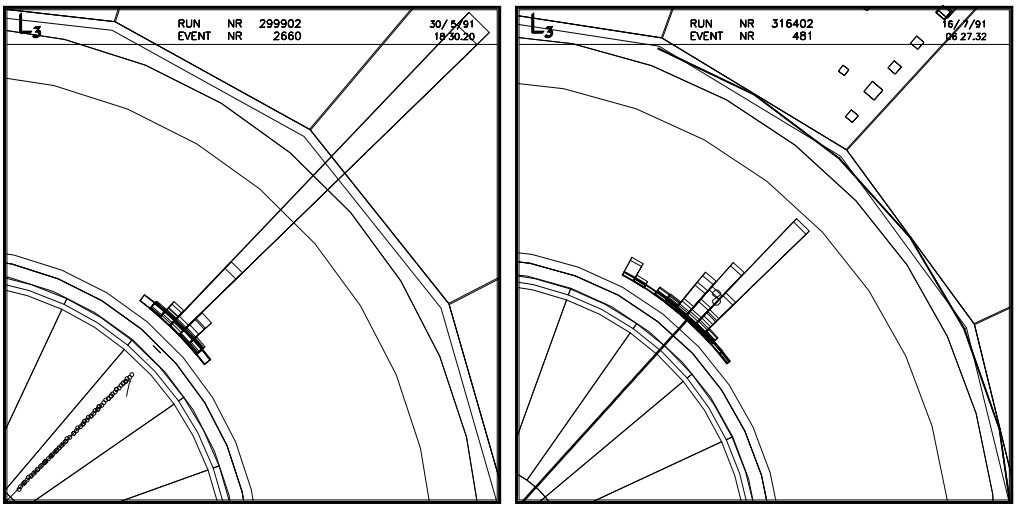

Figure 3.1: Comparison of electron and pion candidates, showing their characteristic profile in the BGO calorimeter, the relationship between the TEC track and shower maximum, and the energy deposition in the hadron calorimeter.

3.1.2 Electron identification

The following criteria have to be met for a particle to be considered an electron:

- $\chi^2_{\mathrm{EM}} < 20$ for 8 degrees of freedom.
- The angle between the track and the center of gravity of the shower must be less than 10 mrad in $r - \phi$ and 20 mrad in z.
- The energy deposition in the HCAL behind the shower must be consistent with the tail of an electromagnetic shower.

3.1.3 Charged pion identification

Charged pions are identified with the following requirements:

- The χ^2 is inconsistent with the assumption that it is electromagnetic.
- HCAL deposition is not consistent with a MIP.

- No muon chamber track is matched. Most pions fully interact in the HCAL. If it does punch through, it is of very low energy and scatters in a direction incompatible with the TEC track.

- total BGO and HCAL (and MUCH if punch-through) energy compatible with the track momentum.

3.1.4 Muon identification

Muons can be identified in two ways: by using the muon chambers, or failing that, by using a combination of TEC and calorimeters. A track is identified as a muon if it has hits in the muon chambers, and when extrapolated falls within 5σ of the interaction point. It is also tagged as a muon if there are no muon chamber hits, but the TEC track matches to a MIP-like deposition in the HCAL, and the corresponding BGO cluster has energy below 1 GeV(a MIP leaves about 250 MeV in BGO).

3.1.5 Hadronic enviroment

It is necessary for the analysis to correctly identify as many particles as possible in a hadronic(hence high multipliticity) enviroment. $Z \rightarrow \tau^+\tau^-$ events were used to investigate particle identification and seperation. In particular, $\tau^- \rightarrow \rho$ and the three-pronged $\tau^- \rightarrow a_1$ decay are useful.

$\tau^- \rightarrow \rho$ decay

$\tau^- \rightarrow \rho$ decays often involve overlapping or very close electromagnetic and hadronic showers in the BGO. An iterative approach was developed to deal with these cases, which are very common in hadronic events (see Figure 3.2):

1. The pion impact position is determined from the TEC track.

2. A normalized hadronic shower profile is fitted here(a).

3. This profile is subtracted from the total observed cluster, presumably leaving a neutral electromagnetic profile(b).

4. This neutral cluster is fitted with electromagnetic shower profiles. Multiple EM profiles are used if they fit better(this is often the case with energetic π^0 as the photons are very close to each other)(c).

5. A new hadronic energy is found by subtracting the fitted EM shower profiles from the total visible energy(d).

Steps 2-4 are iterated until all reconstruced energies are stable to within 1%. Typically 3 to 4 iterations are required.

Next the neutral pions are identified. Two seperate photon depositions form a π^0 candidate if their invariant mass falls within 40 MeV of the π^0 mass. One neutral cluster is a π^0 candidate if its energy is above 1 GeV and its χ^2 is below 20, or if two fitted electromagnetic shapes shapes yield an invariant mass within 50 MeV of the π^0 mass.

three-pronged $\tau^- \rightarrow a_1$ decays

The three-pronged $\tau^- \rightarrow a_1$ decays are useful to investigate reconstruction of close tracks. As much 3–D information as possible is needed for this. TEC only gives useful information in the r–ϕ coordinates, so SMD and the Z–chambers are included in the analysis. The single hit Z–chamber resolution is about 300–400 μm. Overlapping hits yield a much larger uncertainty. SMD has a resolution of about 25 μm in the z-direction, and thus provides a significant contribution to the z information. Full SMD and Z-chamber information is used in the reconstruction. A combinatorial procedure is developed by which the tracks are varied among all the z data, and the combination with the smallest χ^2 is picked as the full 3–D event reconstruction.

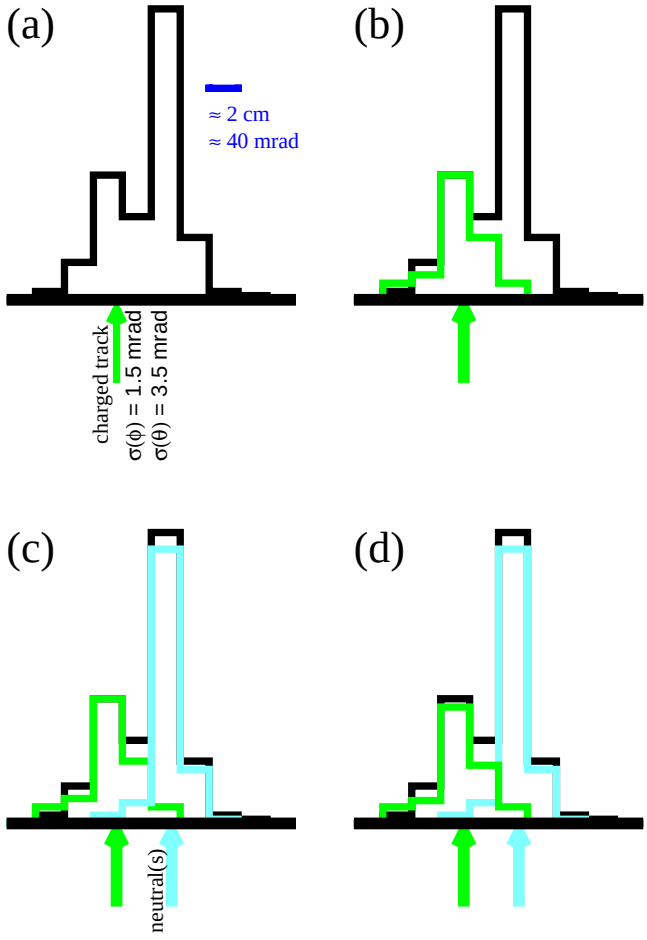

Figure 3.2: Illustration of the procedure used to determine the energies of one charged hadron and several photons from overlapping clusters in the BGO.

Chapter 4

Analysis Technique

In this chapter the main techniques used to search for the $B^- \to \tau^- \overline{\nu}_\tau$ and the $D_s^- \to \tau^- \overline{\nu}_\tau,\ \tau^- \to l^- \overline{\nu}_l \nu_\tau$ decays are explained.

The $D_s^- \to \tau^- \overline{\nu}_\tau,\ \tau^- \to l^- \overline{\nu}_l \nu_\tau$ channel is used to illustrate the procedures. The distinguishing characteristic is that three neutrinos and one lepton are the final particles. Thus the obvious signature for this decay is a high missing energy.

The missing energy property is used to impose a loose preselection to substantially decrease the background by having the transverse energy imbalance $E_\perp/E_{vis}$ be greater than 0.25. The $Z^0 \to u\bar{u}, d\bar{d}, s\bar{s}$ events have hardly any leptonic decays in them and thus the missing energy is very low. On the other hand, the $Z^0 \to c\bar{c}$ and in particular the $Z^0 \to b\bar{b}$ events always involve decays of high mass quarks into lower mass quarks, often leading to leptonic decays. Thus the cut on the transverse energy imbalance will eliminate most $Z^0 \to u\bar{u}, d\bar{d}, s\bar{s}$ and nonleptonic $Z^0 \to c\bar{c}$ and $Z^0 \to b\bar{b}$ events. A further preselection cut on the number of tracks being larger than seven is imposed to ensure that no $Z^0 \to e\bar{e}, \mu\bar{\mu}, \tau\bar{\tau}$ events are selected.

After the preselection the dominant background are the c and b semileptonic decays, as they also can have a large missing energy. These completely swamp the signal. In the case of $D_s^- \to \tau^- \overline{\nu}_\tau$ events the background exceeds the signal by two orders of magnitude. Several techniques are employed to substantially increase the signal component, as described in the following sections.

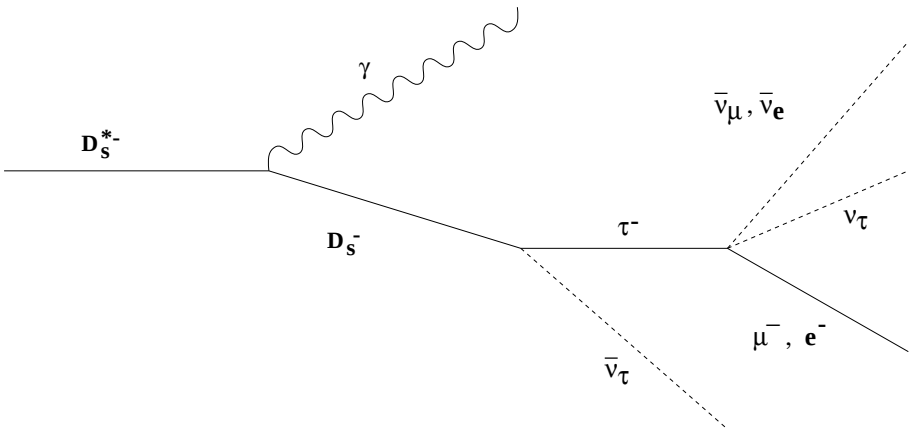

Figure 4.1: Feynman diagram for the decay chain $D_s^{*-} \rightarrow \gamma D_s^-$, $D_s^- \rightarrow \tau^- \overline{\nu}_\tau$, $\tau^- \rightarrow l^- \overline{\nu}_l \nu_\tau$.

4.1 Photon tagging

A useful technique in separating the signal from the background involves photon tagging the D_s^- meson. This method uses the fact that a certain fraction of the D_s^- mesons originate from the excited D_s^{*-}, which promptly decays to a photon and D_s^-.

This is used as a very useful tag by combining the reconstructed D_s^- with the photon as this should lead to a peak at the D_s^{*-} invariant mass. The Feynman diagram for the whole chain is shown in Figure 4.1.

The invariant mass of D_s^{*-} can then be calculated using the reconstructed D_s^- momentum and measured photon momentum

$$M^2_{\gamma D_s^-} = M^2_{D_s^-} + 2P_\gamma P_{D_s^-} \left(\frac{1}{\beta_{D_s^-}} - \cos\theta_{\gamma D_s^-}\right) \tag{4.1}$$

where $M_{\gamma D_s^-}$ is the invariant mass of the D_s^{*-}, $M_{D_s^-}$ the invariant mass of the D_s^-, P_γ the photon momentum, $P_{D_s^-}$ the D_s^- momentum, $\beta_{D_s^-}$ the velocity of the D_s^-, and $\theta_{\gamma D_s^-}$ the angle between the photon and the D_s^- reconstructed direction.

If the selected photon does indeed come from a D_s^{*-} decay then a peak should form at the D_s^{*-} invariant mass. The invariant mass resolution is estimated to be 52 MeV/c^2 for the selected combinations of D_s^- and γ (Figure 4.2).

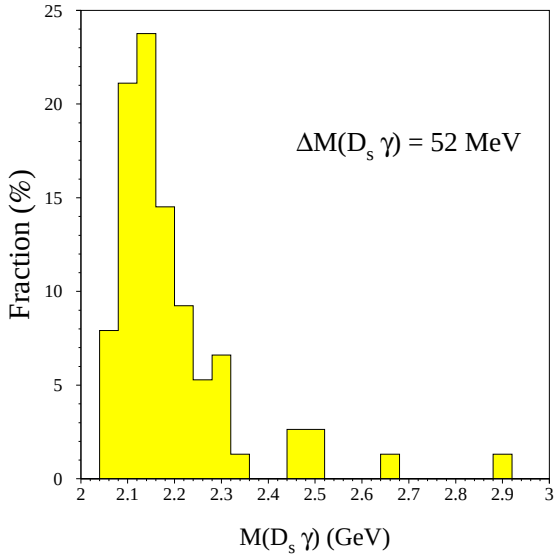

Figure 4.2: $M_{\gamma D_s^-}$ invariant mass distribution for the selected Monte-Carlo events from the decay chain $D_s^{*-} \to \gamma D_s^-$, $D_s^- \to \tau^- \overline{\nu}_\tau$.

4.2 Reconstruction technique

It is possible to substantially reduce the semileptonic background using a fitting procedure with constraints. This reconstruction technique hinges on the fact that only one lepton is the final detectable particle for the searched decays, while there are multiple tracks from semileptonic decays. Energy–momentum conservation is then used to reconstruct the energy and direction of D_s^-:

$$\vec{P}_{D_s^-} = -\sum_{i \neq \text{lepton}} \vec{P}_i \tag{4.2}$$

$$E_{D_s^-} = \sqrt{s} - \sum_{i \neq \text{lepton}} E_i \tag{4.3}$$

The summation is done over all detected particles in both hemispheres of the event:photons, charged and neutral hadrons, except the lepton taken to be a τ decay product. The momenta of the particles are calculated by identifying the

particles as photons, neutral or charged pions, electrons, or muons and then using the corresponding mass.

The energies of all reconstructed particles (E_i^{fit}) are then varied in the kinematic fit to minimise their deviations from the experimentally measured values

$$\chi^2 = \sum_{i \neq lepton} \frac{(E_i^{fit} - E_i^{meas})^2}{\sigma^2_{E_i^{meas}}}, \tag{4.4}$$

under the constraint $\sqrt{E^2_{D_s^-} - \vec{P}^2_{D_s^-}} = M_{D_s^-}$, where the fitted values are used in Equations 4.2 – 4.4.

If the decay is indeed a leptonic $D_s^- \to \tau^- \overline{\nu}_\tau$ decay, then the assumption that the lepton is the only detectable particle originating from the D_s^- is correct and hence the final energy of the D_s^- should not significantly vary from the original one. If on the other hand there is a semileptonic case, then this assumption is wrong. This results in the fitting procedure (Equation 4.4) substantially underestimating the reconstructed momentum of heavy hadrons. Therefore the D_s^- energy spectrum of the background events is softer than the signal one (Figure 4.3). This property of the energy spectrum shifting downwards for the semileptonic decays and not for the leptonic decays is crucial for the background rejection.

The energy and angular accuracy for the D_s^- meson is extracted by comparing the final numbers for the energy and momentum yielded by the fit with the true ones. The energy resolution is $\sigma(E_{D_s^-}) \sim 3.0$ GeV, while the angular accuracy is about 60 mrad.

This is all at the Monte Carlo level. It is necessary to ascertain that same results are yielded by real data. It is of course impossible to use D_s^- events in the data, so a different approach is adopted. A large sample of $Z \to q\overline{q}(\gamma)$ events with a high energy photon is used, with the photon taking the place of the D_s^- meson in the above analysis. Thus the photon is taken out of the fit, and the kinematic constraint is $E_\gamma = P_\gamma$. The resulting plots of the resolution functions are shown in Figure 4.4. As can be seen, the Monte Carlo and data agree very well. The final energy resolution is $\sigma_E = 3.0$ GeV, while the θ and ϕ resolutions are $\sigma_\theta = 61$ mrad and $\sigma_\phi = 53$ mrad, respectively.

A similar procedure is used for $B^- \to \tau^- \overline{\nu}_\tau$ leptonic events, with the invariant mass constraint being M_B and not $M_{D_s^-}$. There is no lepton in the hadronic channel of the $B^- \to \tau^- \overline{\nu}_\tau$ decay, so for this case the track picked is the one with highest impact parameter.

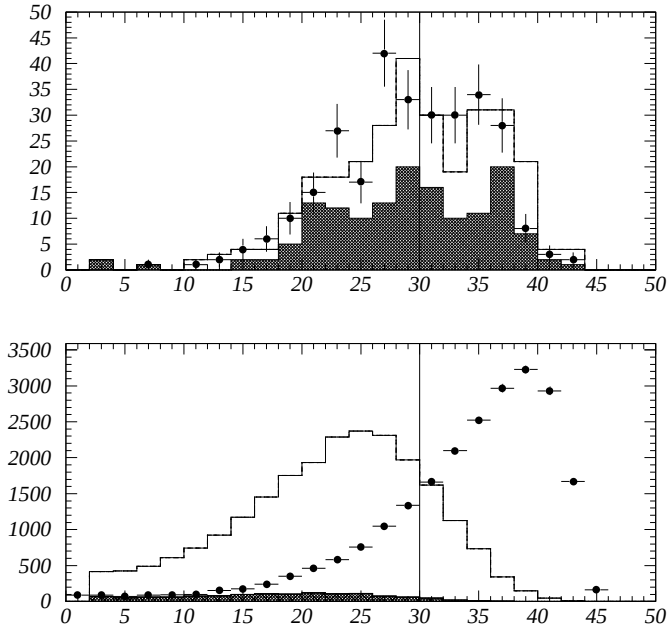

Figure 4.3: Energy spectrum of heavy flavour mesons after the reconstruction (solid histogram) in comparison with their actual energies (dots) for: $D_s^- \to \tau^- \overline{\nu}_\tau$ decays (the hatched area corresponds to the $D_s^{*-} \to \gamma D_s^-$ decays)(top); and for semileptonic decays (the hatched area corresponds to $D^* \to \gamma D$ decays)(bottom).

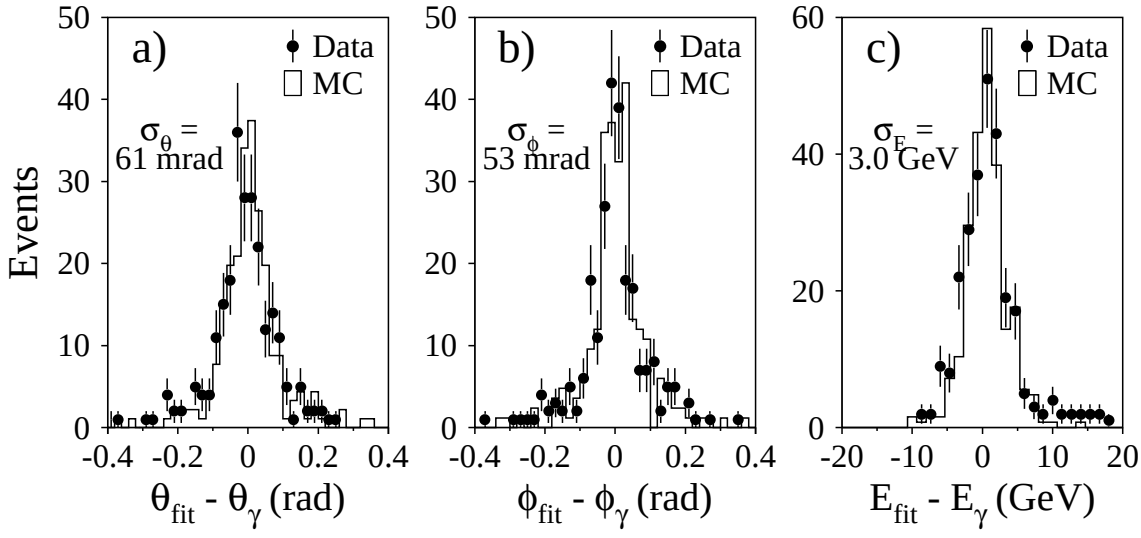

Figure 4.4: Study of the resolution functions using the control sample of $Z \to q\overline{q}(\gamma)$ events: energy resolution (a), polar angle resolution (b) and azimuthal angle resolution (c).

4.3 Impact parameter

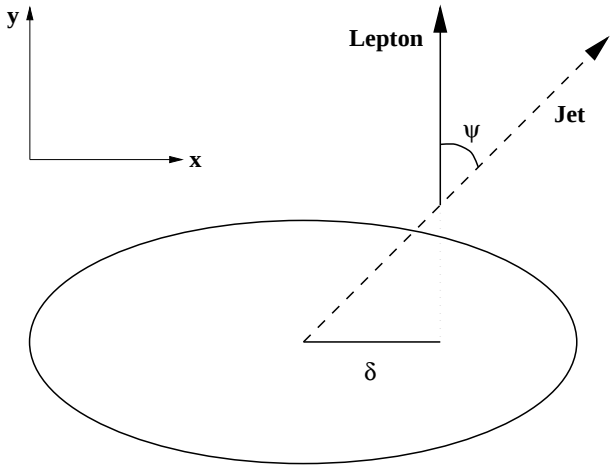

Figure 4.5: Definition of the impact parameter.

A distinguishing feature of c and b decays are their lifetimes. The b mesons are longer lived than the c mesons and this is reflected in a larger separation from the interaction vertex. Hence the so-called impact parameter δ is employed, defined as the absolute value of the distance of closest approach(DCA) with a sign that is positive if the track intersects the direction of the accompanying jet in the direction of the jet's total momentum, negative if it intersects opposite to that direction (see Figure 4.5). Hence an impact parameter distribution for tracks originating at the primary event vertex is symmetric around $\delta = 0$. Its spread is given by the compound effects of a finite beam spot size and multiple scattering, as described below. The impact parameter for tracks coming from long lived particles is thus positive on average.

The multiple scattering is due to berrylium pipes and the SMD between TEC and the interaction point. This contribution to σ_{DCA} can be expressed in terms of the transverse momentum $\mathrm{p}_\perp$ and a single constant:

$$\sigma_{\mathrm{MS}} = \frac{150}{\mathrm{p}_\perp} \tag{4.5}$$

The fill vertex error reflects the shape of the LEP beamspot size. This is oval shaped in the transverse direction, with a resolution of $\sigma_{\mathrm{H}} = 130$ μm in the horizontal direction, and $\sigma_{\mathrm{V}} = 25$ μm in the vertical direction.

Thus the final expression for the DCA resolution is given as:

$$\sigma^2_{\mathrm{DCA}} = \sigma_{\mathrm{MS}} \otimes \sigma_{\mathrm{vertex}} \tag{4.6}$$

$$= \left(\frac{150}{\mathrm{p}_\perp}\right)^2 + \sigma^2_{\mathrm{V}}\mathrm{sin}\phi + \sigma^2_{\mathrm{H}}\mathrm{cos}\phi \tag{4.7}$$

where ϕ is the azimuthal angle.

The ratio of the impact parameter and its error is taken to define the significance s. Figure 4.6 shows the distribution of the significance s after the preselection has been applied. Good agreement between data and Monte Carlo is seen. The difference in the significance s between the b quarks and the rest are clear.

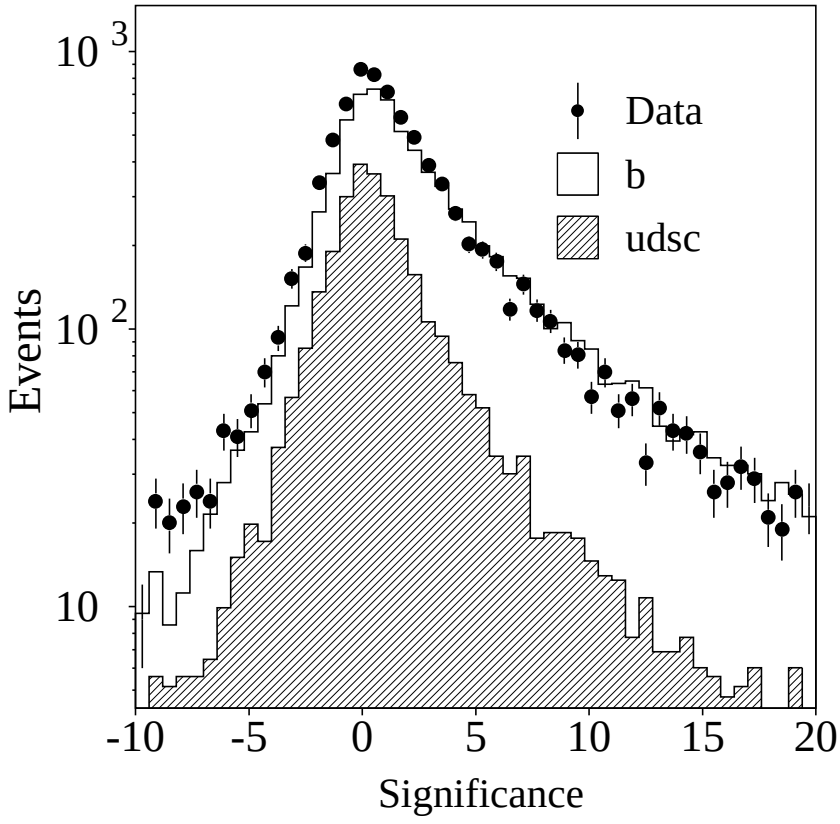

Figure 4.6: Significance distribution of data and Monte Carlo. The hatched histogram represents Monte Carlo contribution of the u, d, s and c quarks, while the open histogram is due to b quarks.

Chapter 5

Measurement of the $\mathrm{D_S^-} \to \tau^- \overline{\nu}_\tau$ Branching Ratio

5.1 Selection of $\mathrm{D_S^-} \to \tau^- \overline{\nu}_\tau$ events

In this section the full methodology used in extracting the $\mathrm{D_s^-} \to \tau^- \overline{\nu}_\tau$ signal from the data sample is explained. Since photon tagging of the $\mathrm{D_s^-}$ is used, then the full searched for chain is:

$$\begin{array}{lllll} c \to \mathrm{D_s^{*-}} \to & \gamma \mathrm{D_s^-} & & \\ & \mathrm{D_s^-} \to & \tau^- \bar{\nu}_\tau & \\ & & \tau^- \to & l^- \overline{\nu}_l \nu_\tau \end{array}$$

Selection of this decay chain $\mathrm{D_s^{*-}} \to \gamma \mathrm{D_s^-}$, $\mathrm{D_s^-} \to \tau^- \overline{\nu}_\tau$, $\tau^- \to l^- \overline{\nu}_l \nu_\tau$ requires a combination of lepton, photon and missing energy in one of the event hemispheres. Other particles in the same hemisphere are assumed to be fragmentation products and are used to reconstruct $\mathrm{E_{D_s^-}}$ from the kinematic fit reconstruction technique.

The preselection described in the previous chapter are passed by 2.2% (33417 events) of the original data sample and by 26% of the Monte Carlo signal sample. The next step consists of selecting events with a well identified muon or electron in the least energetic hemisphere. Further, all the tracks are required to have a

significance $s < 3$ of their impact parameter to reduce the large b semileptonic background (see Figure 4.6).

The remaining events undergo the kinematic fit reconstruction technique to extract the energy of the presumed D_s^- particle. The mass of the D_s^- is fixed at 1.97 GeV. A cut of $E_{D_s^-} > 30$ GeV is then employed, as indicated in Figure 4.3. This lowers the signal efficiency to 7.3% (from 26%), but is a crucial step in the background suppression as this gets reduced to 0.02% (from 2.2%). To eliminate misreconstructed signal and background events, the identified lepton is required to have a momentum in the D_s^- rest frame below 2 GeV.

In semileptonic D decays the c quark decays to an s or d quark, which differ by a unit charge from the parent quark. Thus the resulting meson from the s or d quarks will have a charge opposite to that of the lepton, as illustrated in Figure 5.1. This meson will in general be very energetic compared to fragmentation particles, as it comes directly from the primary particle. This is shown in Figure 5.2, where the energy spectrum of the most energetic hadron with a charge opposite to the lepton for $D_s^- \to \tau^- \overline{\nu}_\tau$ decays and semileptonic $D \to X\ell^+\nu$ decays is plotted. Hence the large D semileptonic background can be reduced by requiring that the energy of the most energetic charged particle with a charge opposite to that of the lepton be smaller than 3 GeV.

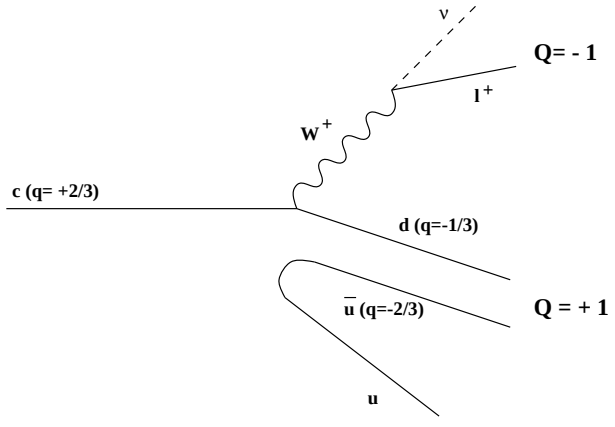

Figure 5.1: Feynman diagram illustrating that in semileptonic decays the resulting meson has a charge opposite to that of the lepton.

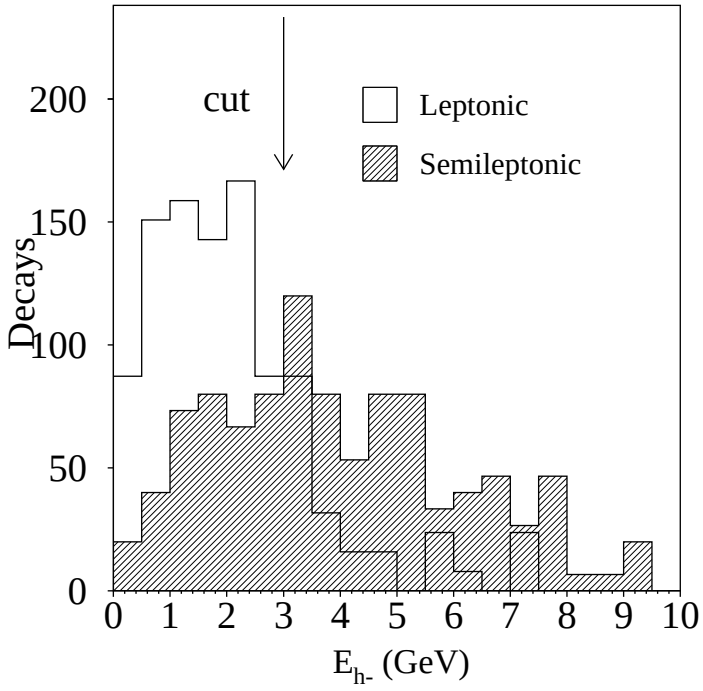

Figure 5.2: energy spectrum of the most energetic hadron with a charge opposite to the lepton for $D_s^- \to \tau^- \overline{\nu}_\tau$ decays (full histograms) and semileptonic $D \to X\ell^+\nu$ decays (hatched histogram).

At this stage photon tagging is employed to extract the signal. There are usually numerous photons in a hadronic event, mostly from π^0 decays. These create a difficulty in finding the correct one. Thus some selection is necessary to suppress the resulting combinatorial background. The most important cut is a lower energy cut of 3 GeV, as the typical photon momentum from $D_s^{*-} \to \gamma D_s^-$ decays is harder than the momentum of photons from π^0 decays. This is illustrated in figure 5.3, where the energies of photons at the Monte Carlo generator level for background and signal events are plotted on a logarithmic scale. This plot also shows that there are no photons above 5 GeV for $D_s^- \to \tau^- \overline{\nu}_\tau$ events. Hence the photon energy is required to be within the $3 \to 5$ GeV window. Further, it must

not form a π^0 (within 20 MeV of the π^0 invariant mass) with any other photon in the hemisphere of at least 0.1 GeV. Occasionally multiple photons pass these cuts. In that case the procedure is to take the more energetic one. As can be seen from Figure 5.4, there is good agreement for the photon energy distribution between data and Monte Carlo before and after the cuts. These cuts further lower the signal detection efficiency to 2%, but are necessary to extract the signal from the background.

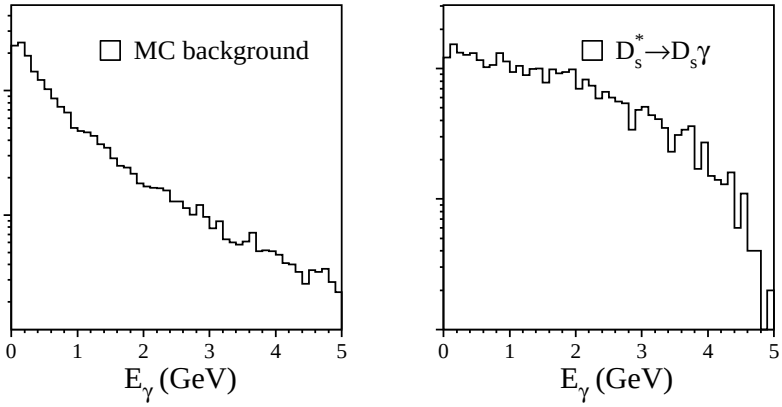

Figure 5.3: Generator level photon energies for background and D_s^{*-} events

The distribution of the $M_{\gamma D_s^-}$ for the events satisfying the selection criteria is shown in Figure 5.5. Also plotted are the expected background and the fitted signal contribution. The peak region ($M_{\gamma D_s^-} < 2.3$ GeV) of Figure 5.5 is occupied by 35 muon and 12 electron candidates in the data. This is in agreement with Monte-Carlo expectations as the efficiency for $\tau^- \to e^- \overline{\nu}_e \nu_\tau$ decays is found to be 2.5 times lower than efficiency for the $\tau^- \to \mu^- \overline{\nu}_\mu \nu_\tau$ channel. The efficiency difference is due to easier identification of muons than electrons, as the muons in muon chambers are in a relatively clean environment, while the electrons at the BGO are in a very contaminated hadronic surrounding. There are several sources which contribute to the signal. The main one is the searched for $D_s^{*-} \to \gamma D_s^-$, $D_s^- \to \tau^- \overline{\nu}_\tau$; it amounts to 81% of the signal. The remaining 19% of the signal comes from $D_s^{*-} \to \gamma D_s^-$, $D_s^- \to \mu^- \overline{\nu}_\mu$ decays as estimated from the partial decay width (Equation 1.23) and

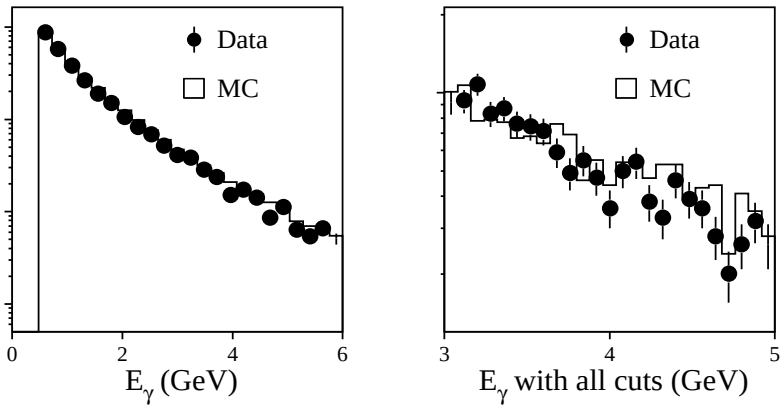

Figure 5.4: Photon energies for data and MC background events before and after the cuts

from the corresponding selection efficiency for this decay mode. A further source to the signal is the decay chain $D^{*-} \to D^- \pi^0/\gamma$, $D^- \to \mu^- \bar{\nu}_\mu$ and $D^- \to \tau^- \bar{\nu}_\tau$. But this contributes only 0.16 decays and is thus negligible. A binned maximum-likelihood fit is used to extract the number of $D_s^{*-} \to \gamma D_s^-$, $D_s^- \to \tau^- \overline{\nu}_\tau$ decays. The background shape and normalisation are fixed in the fit to the Monte Carlo prediction. The fit yields $N = 15.6 \pm 6.0$ for the number of these decays. The error quoted results from the fit and hence is purely statistical.

A peak centred at approximately 2.1 GeV is clearly visible. This agrees very well with the true invariant mass of the D_s^{*-} of 2.110 ± 0.0019 GeV [26]. It is thus justified to call this evidence for the detection of the $D_s^- \to \tau^- \overline{\nu}_\tau$ decay.

A typical candidate event for the decay chain $D_s^{*-} \to \gamma D_s^-$, $D_s^- \to \tau^- \overline{\nu}_\tau$, $\tau^- \to \mu^- \overline{\nu}_\mu \nu_\tau$ is presented in Figure 5.6. The muon and the photon from the decay are shown, together with their measured energies. The muon signature consists of a track in TEC and corresponding MIP-like behavior in the HCAL. The photon is characterized by a large energy bump in the ECAL, with no corresponding TEC track.

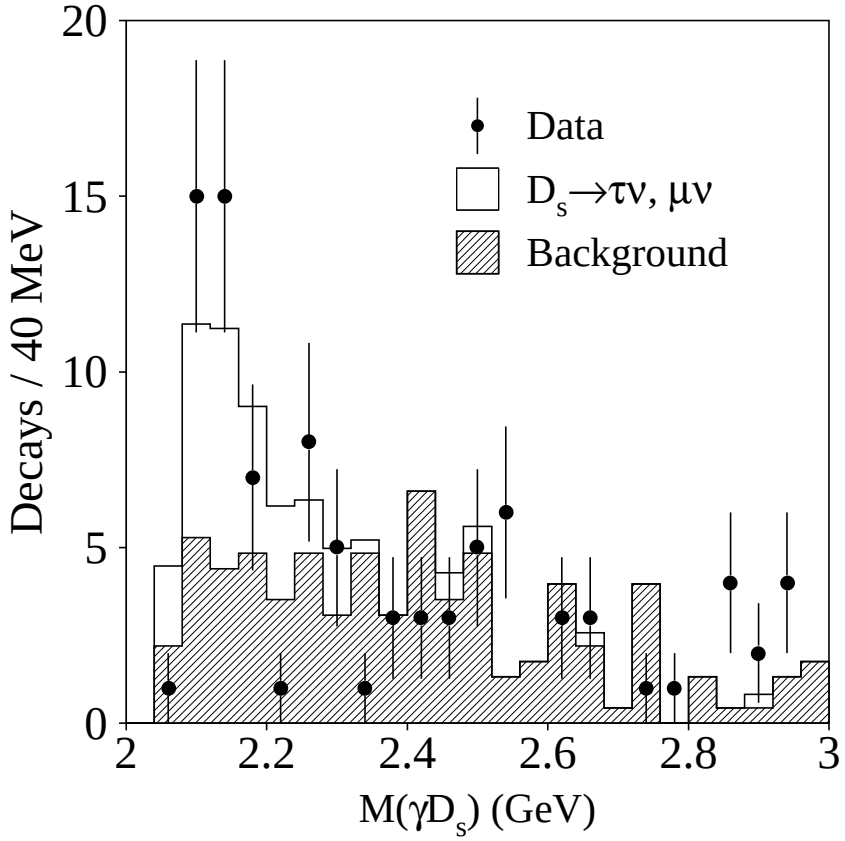

Figure 5.5: The invariant mass distribution, $M_{\gamma D_s^-}$, for the selected events. The hatched histogram represents Monte Carlo estimates for the background, the open histogram shows the fitted signal.

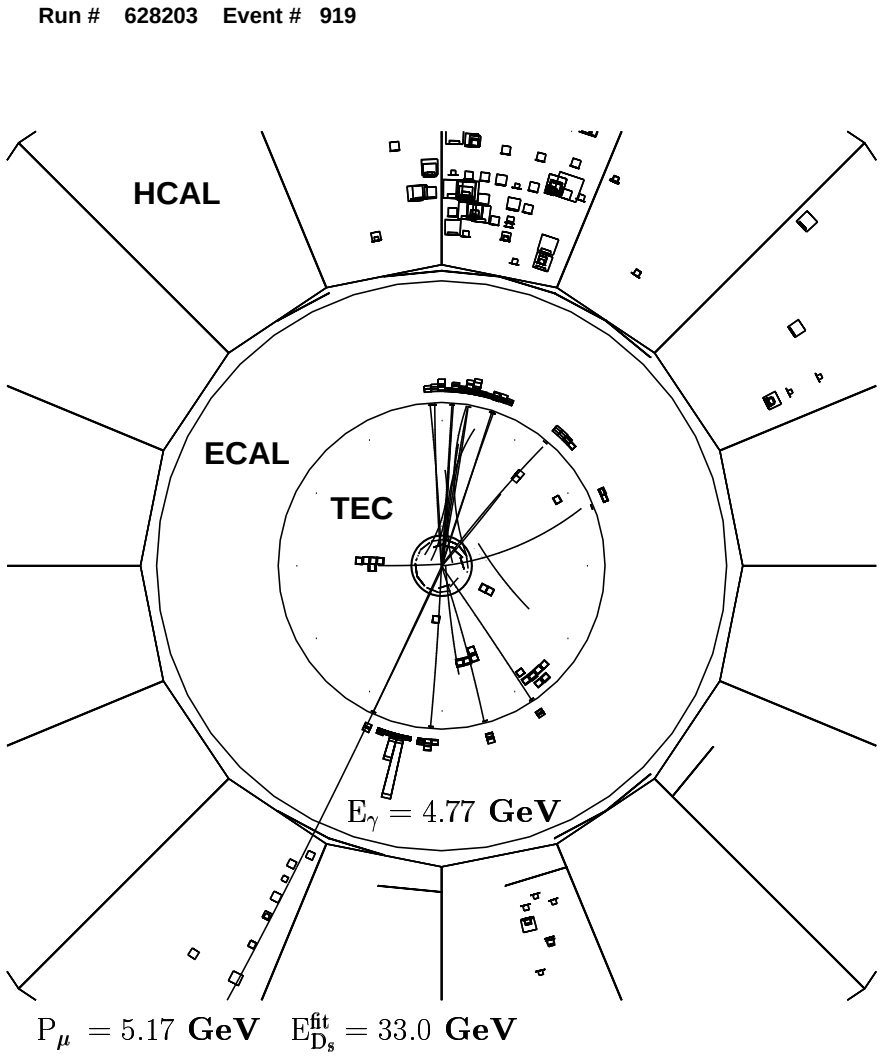

Figure 5.6: candidate event for the decay chain $D_s^{*-} \to \gamma D_s^-$, $D_s^- \to \tau^- \overline{\nu}_\tau$, $\tau^- \to \mu^- \overline{\nu}_\mu \nu_\tau$

5.2 Crosschecks

A peak results only for genuine $D_s^- \to \tau^- \overline{\nu}_\tau$ decays since the opening angle $\theta_{\gamma D_s^-}$ from equation 4.1 obeys kinematic constraints arising from the small mass difference of D_s^{*-} and D_s^- mesons. If this condition is not satisfied then no peak should result. This is used to perform several crosschecks to ensure that the $M_{\gamma D_s^-}$ peak is a real one, and not the result of some quirk in the analysis procedure. Figure 5.7 shows the invariant mass of $M_{\gamma D_s^-}$ for the case when the energy of the most energetic charged particle with a charge opposite to that of the lepton is smaller than 3 GeV and when it is larger than 3 GeV. The photon energy is required to exceed 2.5 GeV. A clear peak is present only when this energy is lower than 3 GeV. If the peak of Figure 5.5 was a fake one then it is expected that it would show up in the $M_{\gamma D_s^-}$ plots for both energy ranges.

Further,a plot of the D_s^{*-} invariant mass for different regions of the photon momenta is shown in Figure 5.8. In the momenta regions where the signal is swamped by the background ($E_\gamma < 3$ GeV and $E_\gamma > 5$ GeV) there is no indication for a peak, while in the selected regions one has a noticeable event imbalance around the D_s^{*-} invariant mass.

Figure 5.9 shows the distribution of the invariant mass $M_{\gamma D_s^-}$ for different ranges of the D_s^- energy for signal and background Monte Carlo events, and data. The data only shows a peak for $E_{D_s^-} > 30$ GeV, i.e. only in the region where background events do not swamp true D_s^- events.

All these factors lead to the conclusion that unambiguous evidence for $D_s^- \to \tau^- \overline{\nu}_\tau$ decays has been found. The next step is to determine the branching fraction. This involves fitting the peak and determining the contribution due to statistical and systematic errors.

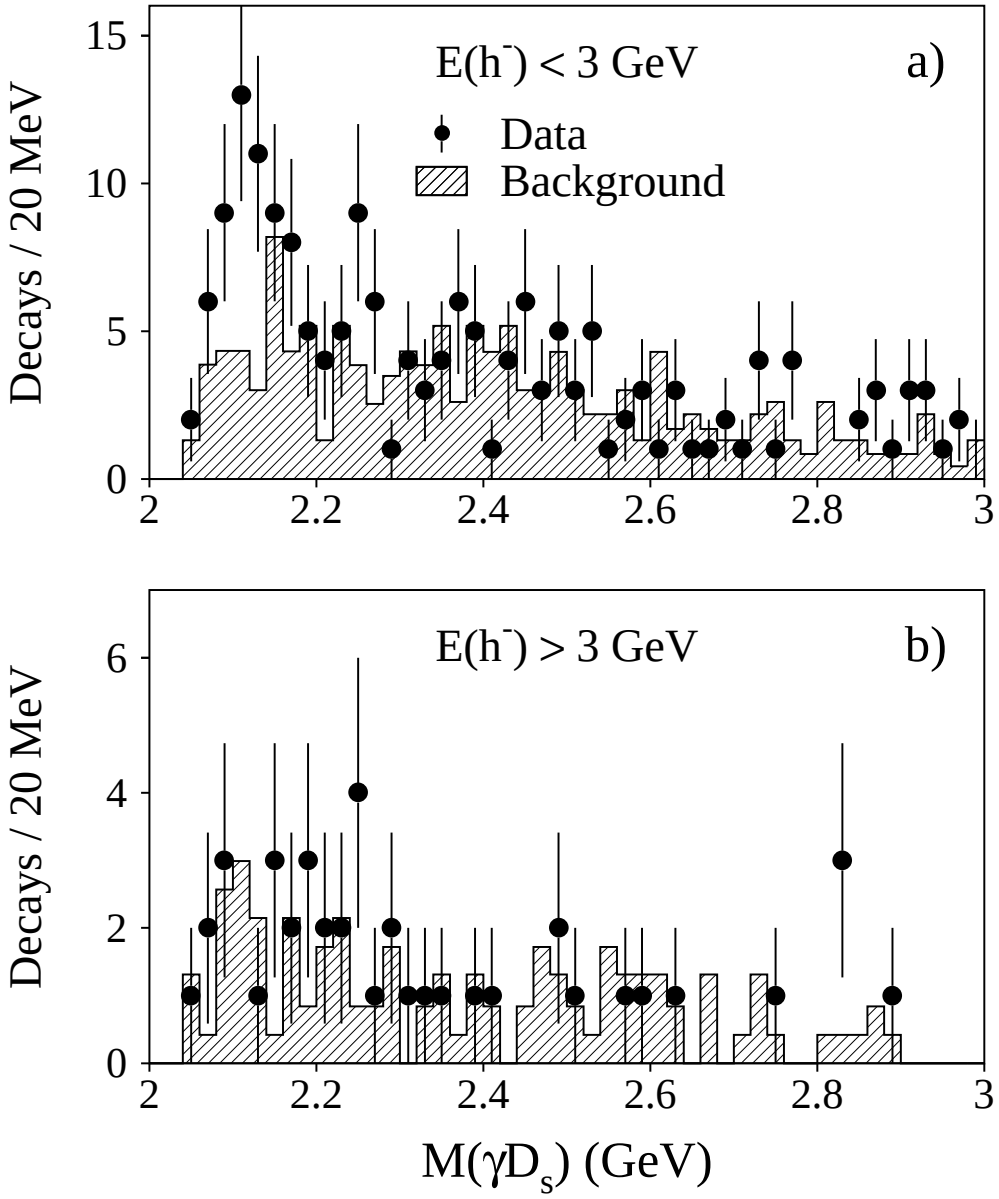

Figure 5.7: Invariant mass distributions, $M_{\gamma D_s^-}$, for two data samples corresponding to two energy ranges of the most energetic particle with a charge opposite to that of the lepton. Photon energy is required to exceed 2.5 GeV. The hatched histogram represents Monte Carlo estimates for the background.

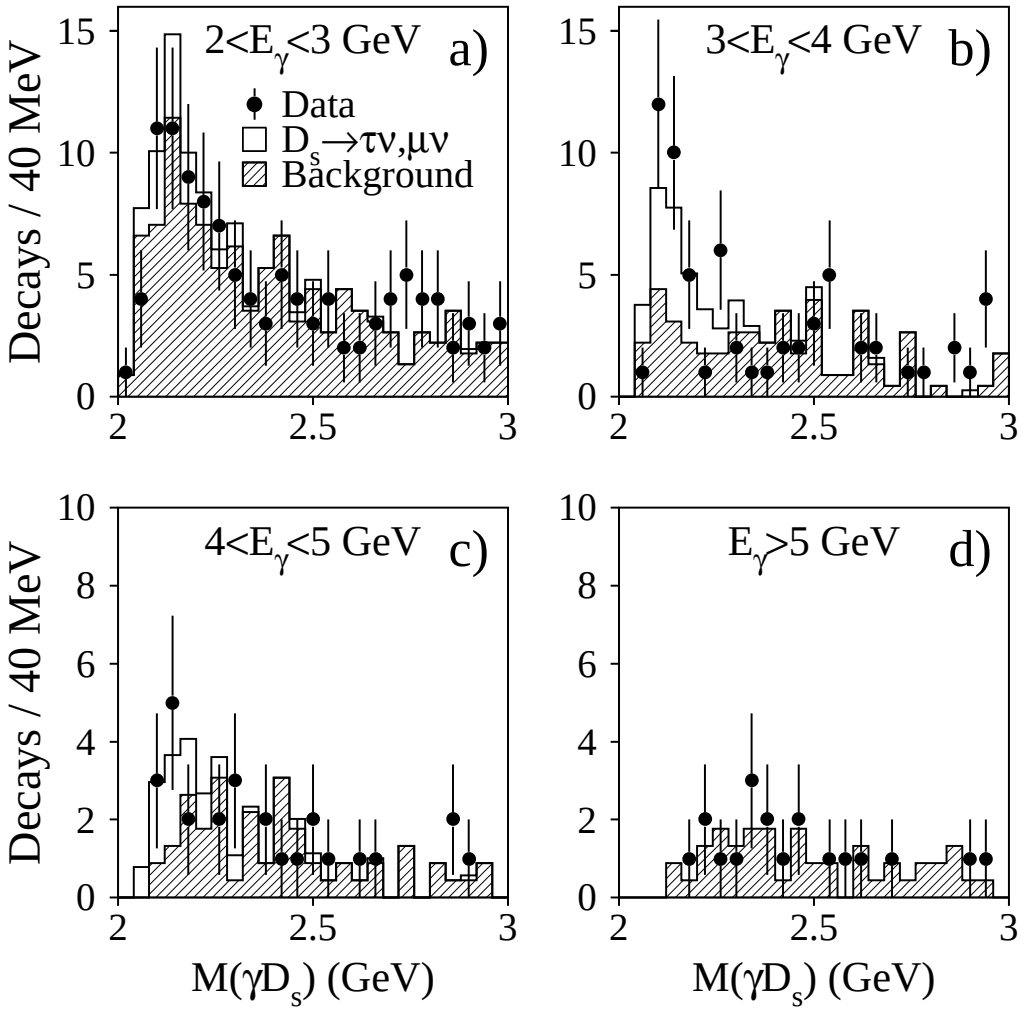

Figure 5.8: Invariant mass distributions, $M_{\gamma D_s^-}$, for the different E_γ ranges.

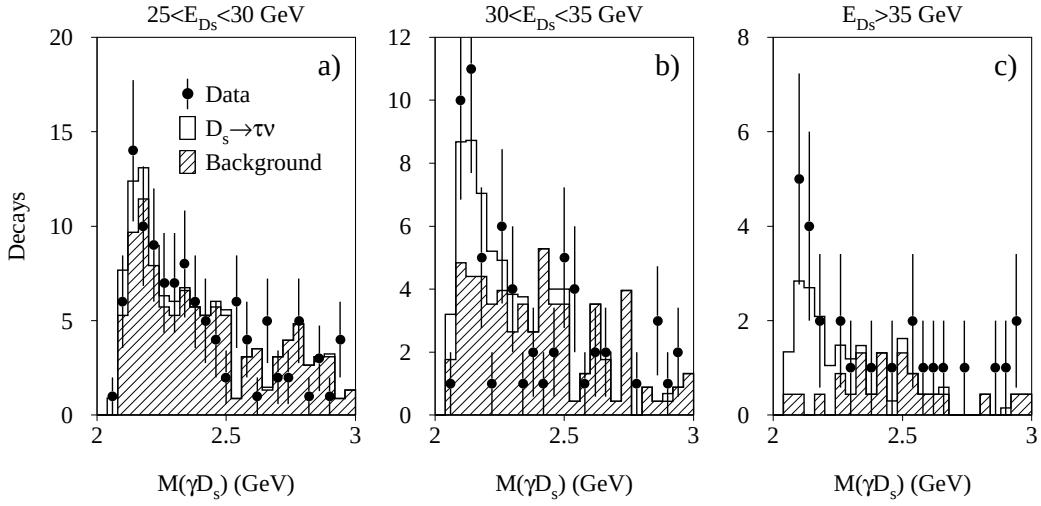

Figure 5.9: Invariant mass distributions, $M_{\gamma D_s^-}$, for the different $E_{D_s^-}$ ranges.

5.3 Systematic errors for the $D_s^- \to \tau^- \overline{\nu}_\tau$ channel

A detailed study is performed of the systematic errors of the measurement. These are determined by averaging the two variations resulting from changing the parameter controlling the error source under consideration by plus or minus one standard deviation of its uncertainty. Each parameter is varied independently. The variation ranges are derived from various sources like PDG [26] or the LEP Electroweak Working Group. All sources are assumed to be independent.

Briefly, the sources of systematic errors are

- uncertainty in the detector resolution function
- uncertainty in the background normalisation
- uncertainty in the shape of the c quark and b quark fragmentation functions
- contribution of the $D_s^{*-} \to \pi^0 D_s^-$ decay
- uncertainty in the D_s^*/D_s fraction
- uncertainty in the D_s/c fraction

If the detector resolution function is not correctly determined, then this has consequences on how many signal decays end up in the peak region. The error due to the uncertainty in the detector resolution function can be found by reweighting the Monte Carlo signal shape using the results of $Z \to q\overline{q}(\gamma)$ study (see Figure 4.4).

Background normalisation errors arise due to the limited knowledge of the branching fractions of the main background channels. These are $\mathcal{B}(D^- \to K^0 l^- \bar{\nu}_l)$, $\mathcal{B}(B_s^{*0} \to B_s^0 \gamma \to D_s^- l^- \bar{\nu}_l X)$, and $\mathcal{B}(D^{*0} \to D^0 \gamma \to K^* l^- \bar{\nu}_l)$. They were varied according to the uncertainties in the PDG values for these decay modes.

For c quark fragmentation, the systematic contribution is obtained by a variation of the fragmentation parameter ϵ_c such that the average energy fraction $< X_E^c >$ changes by $< X_E^c >= 0.49 \pm 0.01$. This mostly affects the signal efficiency.

For b quark fragmentation, the systematic contribution is obtained by a variation of the fragmentation parameter ϵ_b such that the average energy fraction $< X_E^b >$ changes by $< X_E^b >= 0.71 \pm 0.01$. This affects the background efficiency only.

The analysis assumed that 100% of the D_s^{*-} decay to γD_s^-. However, there is a contribution from the isospin violating decay $D_s^{*-} \to \pi^0 D_s^-$. The branching

fraction has been measured to be $\mathcal{B}(D_s^{*-} \to \pi^0 D_s^-) = 0.062\ ^{+0.020}_{-0.018} \pm 0.022$ [27]. This reduces by $(4 \pm 2)\%$ the overall efficiency of $\eta = 0.017 \pm 0.003$(stat) for the studied decay(the fragmentation process $\bar{c} \to D_s^{*-}$ followed by the decay sequence $D_s^{*-} \to \gamma D_s^-$, $D_s^- \to \tau^- \overline{\nu}_\tau$, $\tau^- \to l^- \overline{\nu}_l \nu_\tau$).

The error on the branching fraction $\bar{c} \to D_s^{*-}$ is a further source of uncertainty. This cannot be measured directly, but is calculated from the fraction of D_s^- produced in the c quark fragmentation, and on the fraction D_s^{*-}/D_s^-. The D_s/c fraction is 0.11 ± 0.02 [28–31]. The D_s^{*-}/D_s^- fraction is calculated to be 0.65 ± 0.10 [10, 32]. Spin-consideration in the spectator model of heavy quarks predicts this ratio to be 0.75. QCD string models are then employed to calculate the corrections [33]. These two uncertainties are referred as normalisation errors, as they reflect the lack of knowledge of the actual number of D_s^- mesons produced. This yields a $\bar{c} \to D_s^{*-}$ branching fraction of 0.071 ± 0.017.

A summary of the systematic errors is given in Table 5.1.

5.4 Result of the $D_s^- \to \tau^- \overline{\nu}_\tau$ analysis

The final result for the number of $D_s^- \to \tau^- \overline{\nu}_\tau$ events is
$N = 15.6 \pm 6.0(\text{stat}) \pm 3.4(\text{syst}) \pm 3.7(\text{norm})$. Hence the branching fraction is determined to be

$$\mathcal{B}(D_s^- \to \tau^- \overline{\nu}_\tau) = \frac{\text{yield}}{\epsilon \times N_{Z^0 \to q\bar{q}} \times \frac{\Gamma_{c\bar{c}}}{\Gamma_{q\bar{q}}} \times \frac{D_s^{*-}}{D_s^-} \times \mathcal{B}(\tau^- \to l^- \overline{\nu}_l \nu_\tau) \times 2} \quad (5.1)$$

$$= \frac{15.6 \pm 6.0(\text{stat}) \pm 3.4(\text{syst}) \pm 3.7(\text{norm})}{0.016 \times 1475000 \times 0.1724 \times 0.65 \times 0.36 \times 2} \quad (5.2)$$

$$= (\,7.4 \pm 2.8(\text{stat}) \pm 1.6(\text{syst}) \pm 1.8(\text{norm})\,)\,\% \quad (5.3)$$

where the first error includes data and MC statistics, the second one represents experimental systematic uncertainties and the third one is due to normalisation uncertainties. The Standard Model prediction for the branching fraction $\mathcal{B}(Z \to c\bar{c}) = 0.1724$ is used [34].

This measurement is a significant improvement on the only previous one by the BES collaboration [12] of $\mathcal{B}(D_s^- \to \tau^- \overline{\nu}_\tau) = (12^{+20}_{-10})\%$.

Systematics		
Parameter	Variation	ΔN
resolution function	$\sigma_{E_{D_s^-}} = 3.0\,\text{GeV}$ $\sigma_{\theta_{D_s^-}} = 61\,\text{mrad}$ $\sigma_{\phi_{D_s^-}} = 53\,\text{mrad}$	1.6
signal efficiency η	0.016 ± 0.003	2.5
fragmentation $< X_E^c >$	0.49 ± 0.01	1.6
fragmentation $< X_E^b >$	0.71 ± 0.01	0.6
$\mathcal{B}(D_s^{*-} \to \pi^0 D_s^-)$	$(6.2 \pm 2.9)\%$	0.3
$\mathcal{B}(D^- \to K^0 l^- \bar{\nu}_l)$	$(6.6 \pm 0.9)\%$	0.4
$\mathcal{B}(B_s^{*0} \to B_s^0 \gamma \to D_s^- l^- \bar{\nu}_l X)$	$(7.6 \pm 2.4)\%$	0.2
$\mathcal{B}(D^{*0} \to D^0 \gamma \to K^* l^- \bar{\nu}_l)$	$(1.3 \pm 0.5)\%$	0.2
Subtotal ΔN		3.4

Normalisation		
Parameter	Variation	ΔN
D_s^*/D_s	0.65 ± 0.10	2.4
D_s/c	0.11 ± 0.02	2.8
Subtotal ΔN		3.7

Table 5.1: Summary of the systematic and normalisation uncertainties

Experiment	$f_{D_s^-}$
WA75(μ)	$223 \pm 45 \pm 20 \pm 47$
CLEO(μ)	$288 \pm 30 \pm 30 \pm 47$
BES($\mu + \tau$)	$430^{+150}_{-130} \pm 40$
E653(μ)	$195 \pm 36 \pm 20 \pm 26$
L3(τ)	$309 \pm 58 \pm 36 \pm 38$

Table 5.2: Summary of $f_{D_s^-}$ measurements

5.5 Determination of $f_{D_s^-}$

The decay parameter $f_{D_s^-}$ is extracted from the branching ratio measurement using Equation 1.23 and the relation $\mathcal{B}(D_s^- \to \tau^- \overline{\nu}_\tau) = \frac{\tau_{D_s^-}}{\hbar}\Gamma(D_s^- \to \tau^- \overline{\nu}_\tau)$, resulting in

$$f_{D_s^-} = 309 \pm 58(\text{stat}) \pm 33(\text{syst}) \pm 38(\text{norm}) \text{ MeV} \tag{5.4}$$

using the PDG values for $\tau_{D_s^-}$, $M_{D_s^-}$ and V_{cs} [26]. This result is compatible with other recent measurements of $f_{D_s^-}$ [9–12].

This result can be combined with other measurements of $f_{D_s^-}$ to arrive at a combined measurement. The summary of all measurements of the decay constant $f_{D_s^-}$ is shown in Table 5.2.

The original results from WA75 [9], CLEO [10], and E653 [11] are corrected for the subsequent changes [26] in the measured values of $\mathcal{B}(D_s^- \to K^+K^-\pi^-)$ and $\mathcal{B}(D^0 \to \mu\nu_\mu X)$, $\mathcal{B}(D_s^- \to \phi\pi^-)$, and $\mathcal{B}(D_s^- \to \phi l\nu_l)$.

The average of all the measurements is derived by first normalizing all the measurements to $\mathcal{B}(D_s^- \to \tau^- \overline{\nu}_\tau)$ using the theoretical prediction of the ratio $\mathcal{B}(\tau\nu_\tau/\mu\nu_\mu) = 9.74$. Then the average is determined with the relationship

$$\mathcal{B}(\tau\nu_\tau) \pm \sigma = \frac{\sum_i w_i \mathcal{B}(\tau\nu_\tau)_i}{\sum_i w_i} \pm (\sum_i w_i)^{-\frac{1}{2}} \tag{5.5}$$

where

$$w_i = \frac{1}{(\sigma_i)^2} \tag{5.6}$$

This yields a value for the $\mathcal{B}(D_s^- \to \tau^- \overline{\nu}_\tau) = (5.33 \pm 0.74)\%$, and $\chi^2/dof = 5.8/4$. The probability to have a χ^2 equal or worse than that due to statistical fluctuations

is 21%. The error on $\mathcal{B}(D_s^- \to \tau^- \overline{\nu}_\tau)$ is thus multiplied by a factor $\sqrt{5.8/4}$ using the PDG prescription [26] when extracting the $f_{D_s^-}$ value. The final average for the decay constant $f_{D_s^-}$ is then $f_{D_s^-} = 263 \pm 22$ MeV.

Chapter 6

Measurement of the $B^- \to \tau^- \overline{\nu}_\tau$ Branching Ratio

Selection of the fragmentation and decay chain $Z \to b\bar{b}$, $b \to B^- \to \tau^- \overline{\nu}_\tau$, $\tau^- \to X^- \nu_\tau$ is relatively similar to the $D_s^- \to \tau^- \overline{\nu}_\tau$ analysis, as many topological properties are the same. There are some important differences though, which are explained below.

It was not possible to extract a clear signal for the searched decay. Instead, an upper limit for the $\mathcal{B}(B^- \to \tau^- \overline{\nu}_\tau)$ is arrived at. To improve this value both the leptonic and hadronic channels of $B^- \to \tau^- \overline{\nu}_\tau$ decays have been separately analysed.

6.1 Leptonic channel

First, a τ decay candidate is selected in the least energetic event–hemisphere. The decay is identified by the presence of a lepton of at least 1 GeV momentum [25]. The associated track is required to be at least 5σ away from the primary vertex in the plane perpendicular to the beam direction. This significantly reduces the non-$Z^0 \to b\bar{b}$ background since the B-meson is very long lived compared to the mesons formed from the lighter quarks (Figure 4.6). Figure 6.1 shows this distribution for the selected lepton after all the other cuts have been applied.

This particle is not used in the kinematic fit for the B^- energy and direction. The resulting energy distribution is shown in Figure 6.2. The reconstructed energy of the B^- must exceed 30 GeV. All other tracks in the same hemisphere are required

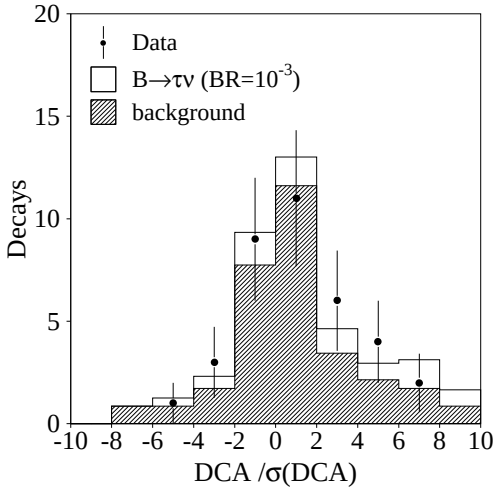

Figure 6.1: The final distribution of the significance for leptonic $B^- \to \tau^- \overline{\nu}_\tau$ events

to be consistent with the primary vertex within 3σ in the transverse plane.

It is not possible to use a photon to tag decays of the type $B^{*-} \to B$, even though about 76% [35] of B_s^- come from the B^{*-} meson. This is because the mass difference between a B^{*-} and a B^- is only about 46 MeV. Thus in the lab frame the average photon energy is around 500 MeV, and virtually never exceeds 800 MeV. Hence the photon is completely swamped by the background. This makes the searched decay much harder to find and extra cuts are needed to reduce the background.

The total energy in the hemisphere minus the lepton energy should be small for $B^- \to \tau^- \overline{\nu}_\tau$ events, as only fragmentation particles are involved. This is shown in Figure 6.3, together with the background. An upper cut of 8 GeV is imposed on this energy difference.

One large background source comes from semileptonic decays involving K^0 which can decay in the hadron calorimeter and hence the energy may occasionally not be well measured. In particular, it can get underestimated and thus lead to a large missing energy. To eliminate this no neutral hadron clusters with energy greater than 0.5 GeV are allowed in the 0.5 rad half-angle cone around the reconstructed B direction.

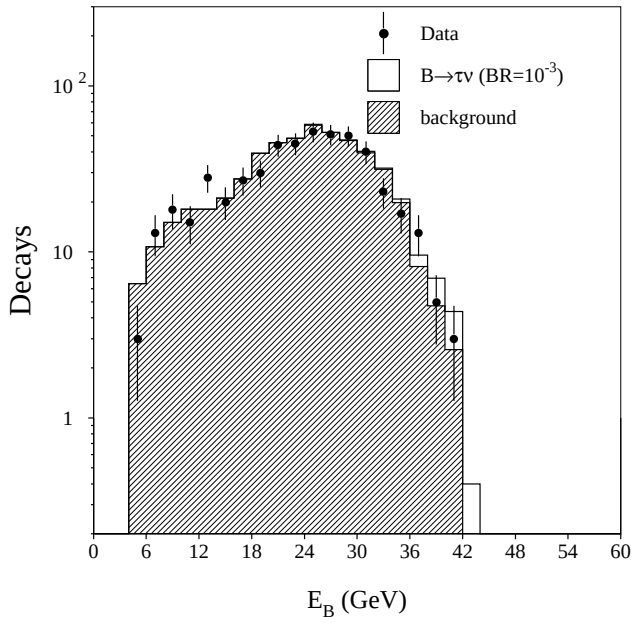

Figure 6.2: Energy spectrum of B^- mesons for the preselected events. The hatched histogram represents the background, the open histogram shows the fitted signal contribution.

The energy spectrum of selected leptons is presented in Figure 6.4. The specific background shape is mostly due to the selection cuts requiring very energetic B^- and little hadronic activity thus leading to preferential selection of high energy leptons from the semileptonic decays. On the other hand for genuine $B^- \to \tau^- \overline{\nu}_\tau$ decays the selection efficiency is reasonably flat in the energy range from 1 to 10 GeV.

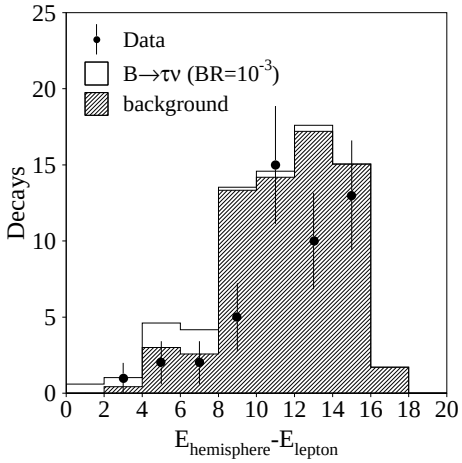

Figure 6.3: Energy in the lower energy hemisphere minus the energy of the selected lepton for data, background, and $B^- \to \tau^- \overline{\nu}_\tau$ events.

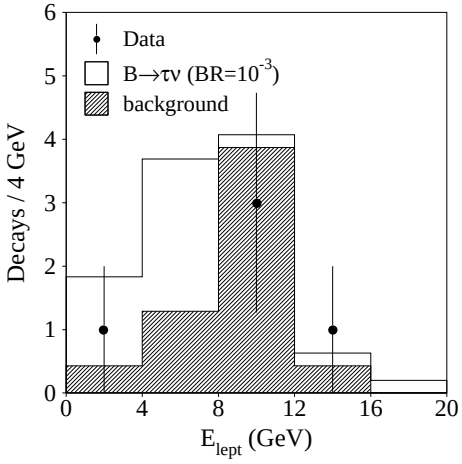

Figure 6.4: Lepton energy spectrum for the selected $B^- \to \tau^- \overline{\nu}_\tau$, $\tau^- \to l^- \overline{\nu}_l \nu_\tau$ candidates. The hatched histogram represents the background, the open histogram shows the signal contribution assuming $\mathcal{B}(B^- \to \tau^- \overline{\nu}_\tau) = 10^{-3}$.

It is important to note that due to the $\mathcal{P}_\tau = +1$ in the $B^- \to \tau^- \overline{\nu}_\tau$ decays the leptons from τ decays are expected to populate preferentially the low energy region. This can be seen by analysing Figure 6.5, where a comparison of τ decays for positive and negative helicities is shown for cases in which the lepton has maximal energy in the τ rest frame. In these cases the neutrinos are emitted in the same direction, opposite to that of the charged lepton. Let the flight direction of the charged lepton define the z-axis. In the cases shown in the figure, there is no orbital angular momentum component along the z-axis, and the z-components of the neutrino spins sum to zero. So for $\lambda_\tau = +1/2$, conservation of the z-component

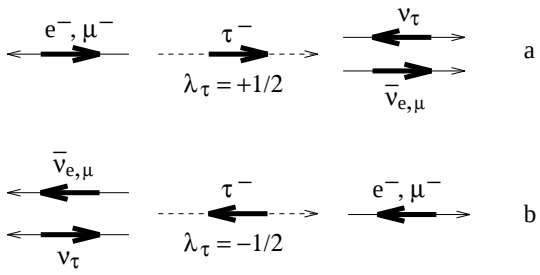

Figure 6.5: Favoured spin and momentum configurations in $\tau^- \to e^- \overline{\nu}_e \nu_\tau$ and $\tau^- \to \mu^- \overline{\nu}_\mu \nu_\tau$ for the case in which the charged lepton has maximal energy in the τ rest frame. The dashed line is the axis defined by the τ flight direction, and the thick arrows indicate the spins.

of angular momentum and the fact that the e^- or μ^- is left-handed favour the configuration shown in Figure 6.5a, in which the charged lepton is emitted in the direction opposite to the flight direction of the τ. On the other hand, for $\lambda_\tau = -1/2$ the most favoured configuration has the charged lepton emitted along the τ flight direction, as shown in Figure 6.5b. So in the lab frame, the energy of the charged lepton is greater for the $\lambda_\tau = -1/2$ case than for the case $\lambda_\tau = +1/2$. Since B mesons are spin zero particles, then the τ has to have a positive helicity, and hence the resulting lepton will have a low energy. In fact, most will occupy the region below 1 GeV, as shown in Figure 6.6 where the electron distribution is plotted as a function of energy. This considerably lowers the selection efficiency, as below 1 GeV it is not possible to distinguish the leptons from the pions with the L3 detector.

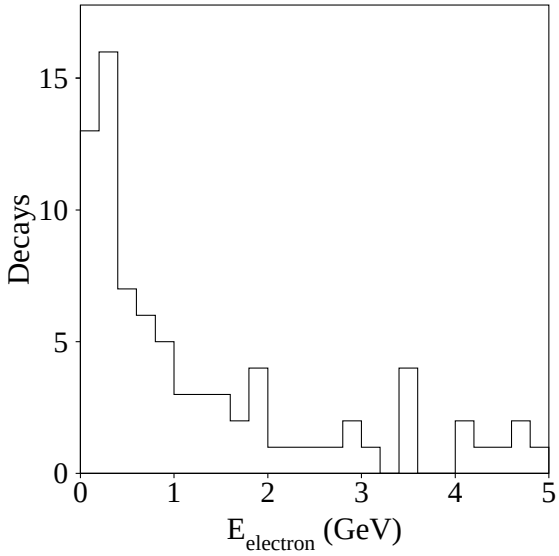

Figure 6.6: Electron distribution of $B^- \to \tau^- \overline{\nu}_\tau$ MC events

6.2 Hadronic channel

Only 36% of the τ particles decay into electrons or muons. The other 64% involve hadronic decays, which have thus been included to improve the upper limit of the $B^- \to \tau^- \overline{\nu}_\tau$ branching ratio.

The hadronic channel is more difficult to analyse than the leptonic one. The tracks from the hadronic τ decays cannot easily be separated from the background, as is the case in the leptonic decays. This makes the choice of the decay track more uncertain.

As before, one track needs to have a DCA significance of at least 5σ, and all the other ones should be within 3σ of the primary vertex. The kinematic fit reconstruction technique is then applied. On top of this, the selection involves cuts on the number of tracks in the least energetic hemisphere, the maximum energy of a particle with same charge as the highest energetic particle, the maximum energy of a particle with opposite charge as the highest energetic particle, and total invariant mass within 0.5 radians of the reconstructed B direction. Figure 6.7 shows these parameters for $B^- \to \tau^- \overline{\nu}_\tau$ and background Monte Carlo events. They are normalised to each other for clarity.

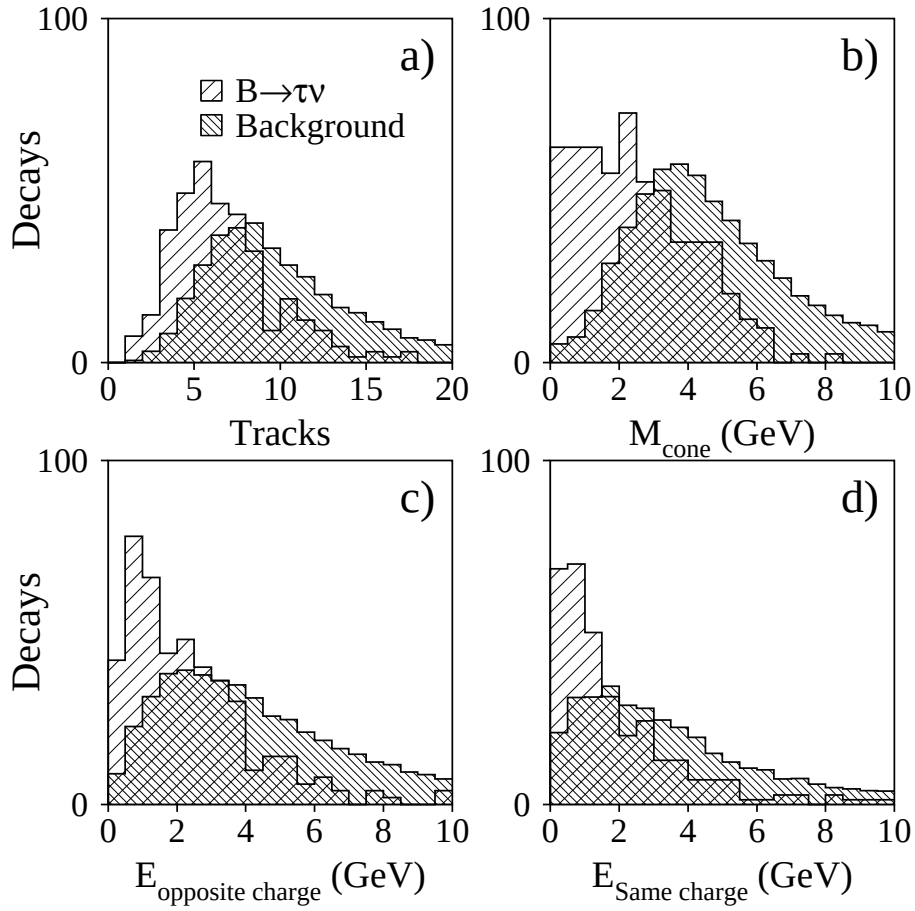

Figure 6.7: Normalised distributions for hadronic $B^- \to \tau^- \overline{\nu}_\tau$ and background Monte Carlo events for a)number of tracks in the lower energy hemisphere, b)invariant mass distribution in the 0.5 rad half-angle cone around the thrust axis, c)energy distribution of the most energetic track with a charge opposite to that of the selected track, and d)energy distribution of the most energetic track with the same charge as that of the selected track.

The hemisphere containing $B^- \to \tau^- \overline{\nu}_\tau$ events is expected to contain a very low track number, as shown in Figure 6.7 a). A maximum number of 5 tracks is imposed.

The invariant mass distribution in the 0.5 rad half-angle cone around the B direction axis is shown in Figure 6.7 b). As expected, the $B^- \to \tau^- \overline{\nu}_\tau$ events have a much smaller resulting invariant mass. An upper cut of 1.25 GeV is set for this parameter.

As explained in the $D_s^- \to \tau^- \overline{\nu}_\tau$ analysis, a true $B^- \to \tau^- \overline{\nu}_\tau$ event will yield low energy tracks if the charge is opposite to the one of the $B^- \to \tau^- \overline{\nu}_\tau$ decay product. Figure 6.7 c) shows the energy distribution of the most energetic track with a charge opposite to that of the selected track. A maximum energy of 2 GeV is imposed. This significantly reduces the semileptonic background. All the other remaining tracks should also be of low energy.

Figure 6.7 d) shows the energy distribution of the most energetic track with the same charge as that of the selected track. The upper cut for this parameter is set at 1 GeV.

The final distributions for the invariant mass and the energy are shown in Figure 6.8. The cut on the invariant mass is indicated in Figure 6.8a.

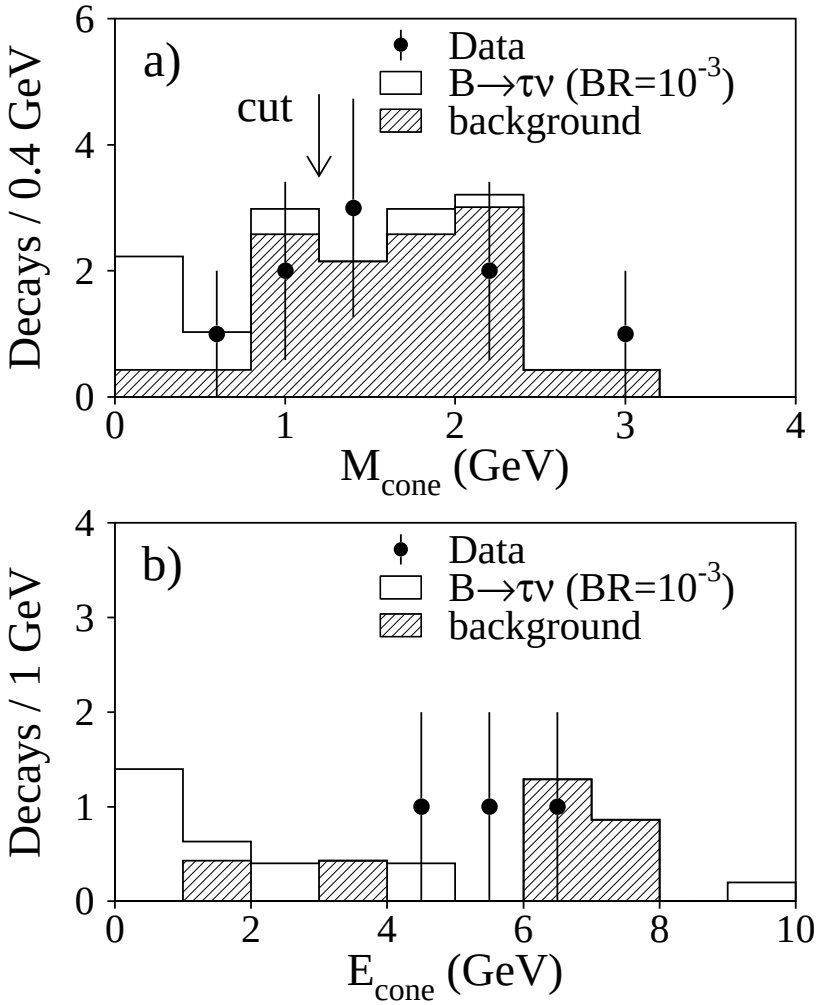

Figure 6.8: Selected candidates for the decay chain $B^- \to \tau^- \overline{\nu}_\tau$, $\tau^- \to \nu X_{hadr}$. The distributions of the invariant mass (a) and total energy (b) for all particles except identified charged τ decay products, in the 0.5 rad half-angle cone around the reconstructed B^- direction. The hatched histogram represents the background, the open histogram shows the signal contribution assuming $\mathcal{B}(B^- \to \tau^- \overline{\nu}_\tau) = 10^{-3}$. Fig (b) shows only events satisfying the cut indicated in Fig. (a).

6.3 Result of the $B^- \to \tau^- \overline{\nu}_\tau$ analysis

The data agree with MC background expectations both for the leptonic and hadronic samples. The likelihood function(Appendix A), used to calculate the upper limit on the number of $B^- \to \tau^- \overline{\nu}_\tau$ decays, accounts for data and Monte Carlo statistics, and uses the data distributions presented in Figures 6.4 and 6.8b.

The dependence of the likelihood function on the number of signal events is shown in Figure 6.9. The upper limit on the number of events due to the contribution from $B^- \to \tau^- \overline{\nu}_\tau$ decays is $N_{B^- \to \tau^- \overline{\nu}_\tau} < 3.8$ at 90% CL. The hadronic channel improves the limit set by the leptonic channel by about 30%. The systematic errors are calculated the same way as for the $D_s^- \to \tau^- \overline{\nu}_\tau$ channel. They are incorporated in the upper limit by smearing the likelihood function with a Gaussian of the appropriate width. However, this contribution to the upper limit turns out to be insignificant.

The overall efficiency for the studied decay is estimated to be $\eta = 0.028 \pm 0.005$ from Monte Carlo simulation. The branching fraction for $b \to B^-$ is taken to be 0.382 ± 0.025 [26]. Using the Standard Model prediction for the branching fraction $\mathcal{B}(Z \to b\bar{b}) = 0.2156$, the following upper limit is obtained

$$\mathcal{B}(B^- \to \tau^- \overline{\nu}_\tau) < 5.7 \times 10^{-4} \text{ at } 90\% \text{ CL} \tag{6.1}$$

This is a significant improvement on the best published limit to date of 1.8×10^{-3} [14].

Using this upper limit in conjunction with Equation 1.24, a limit on the Type II Higgs sector parameter $\tan\beta/M_{H^\pm}$ can be set

$$\frac{\tan\beta}{M_{H^\pm}} < 0.38 \text{ GeV}^{-1} \text{ at } 90\% \text{ CL} \tag{6.2}$$

assuming $f_B = 190$ MeV and using $V_{ub} = 0.0033 \pm 0.0008$ [36].

As can be seen in Figure 6.10, this approaches the best limits on $\tan\beta$ and $M_{H^\pm}$ from the proton stability experiment [37] and from measurements of the $b \to s\gamma$ transition [38].

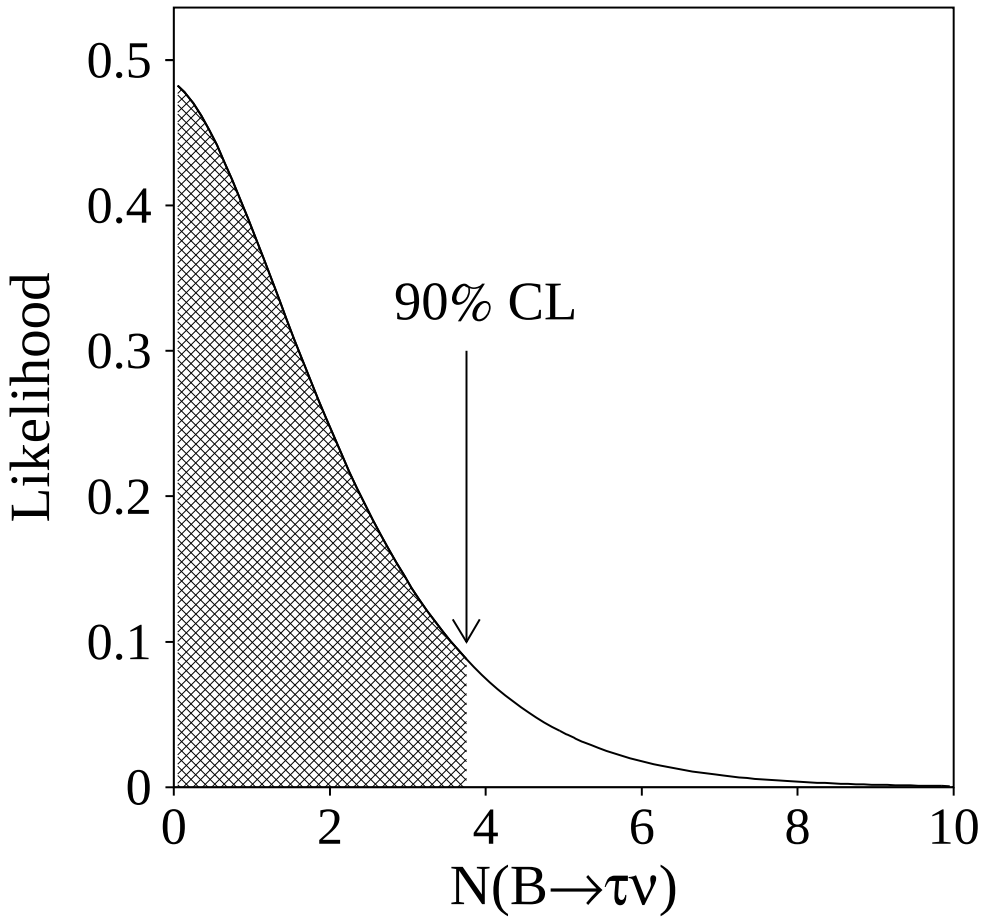

Figure 6.9: Probability density as a function of the number of $B^- \to \tau^- \overline{\nu}_\tau$ events. An upper limit at 90% confidence level corresponds to 3.8 events.

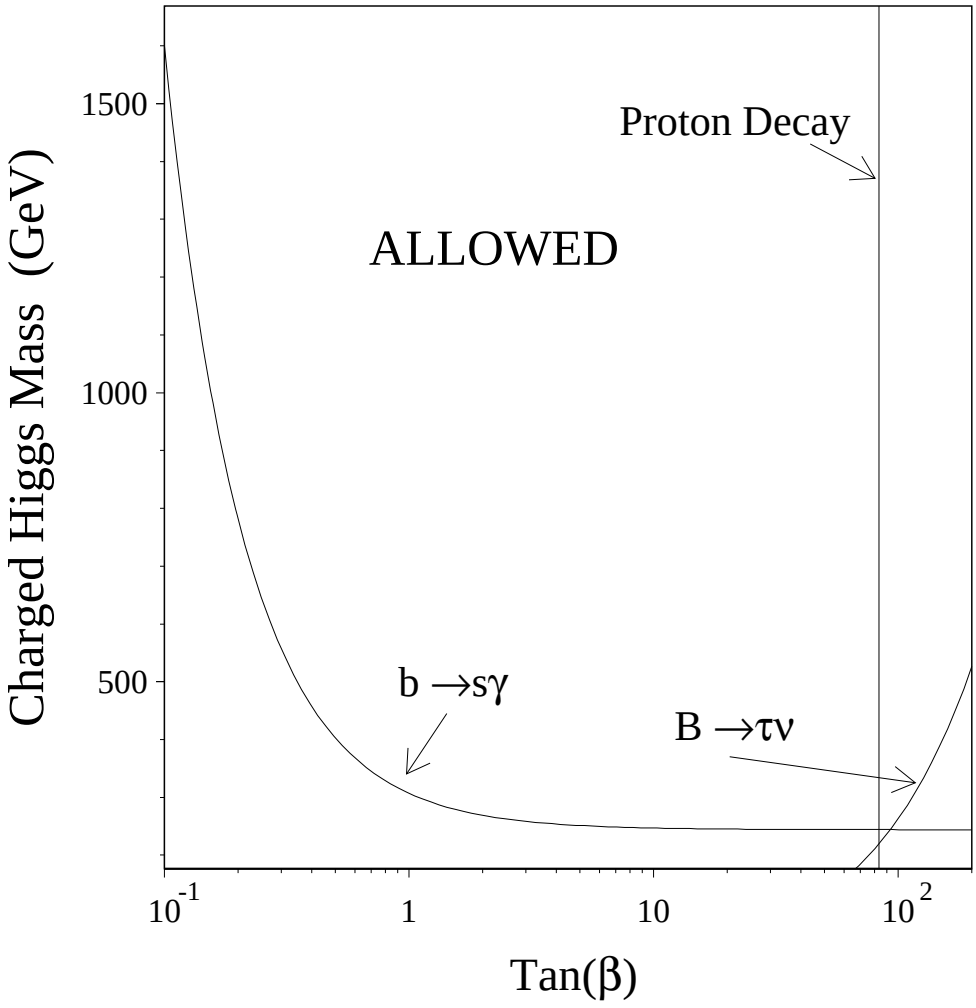

Figure 6.10: Type II Higgs limits

Chapter 7

Conclusion

Excellent separation power of purely leptonic decays from the background in the LEP environment has been achieved using the techniques presented in this analysis. This resulted in the first unambiguous evidence for the $D_s^- \to \tau^- \overline{\nu}_\tau$ channel, and in an improved limit of the $B^- \to \tau^- \overline{\nu}_\tau$ channel. Only data from 1994 has been used. Updated values can thus be obtained by using the full data set. Further, with these techniques the other three LEP experiments will now also be able to achieve improved measurements of purely leptonic decay ratios, leading to very accurate values of $f_{D_s^-}$ in the future. Improved theoretical models should then enable extraction of the f_B decay constant.

7.1 $D_s^- \to \tau^- \overline{\nu}_\tau$ Analysis

Branching ratio for the $D_s^- \to \tau^- \overline{\nu}_\tau$ channel has been measured, corresponding to a value of

$$\mathcal{B}(D_s^- \to \tau^- \overline{\nu}_\tau) = (\, 7.4 \pm 2.8(\text{stat}) \pm 1.6(\text{syst}) \pm 1.8(\text{norm}) \,)\,\% \tag{7.1}$$

This yields a value of the decay constant $f_{D_s^-}$ of

$$f_{D_s^-} = 309 \pm 58(\text{stat}) \pm 33(\text{syst}) \pm 38(\text{norm})\ \text{MeV} \tag{7.2}$$

The improved world average is then

$$f_{D_s^-} = 263 \pm 22\ \text{MeV} \tag{7.3}$$

7.2 $B^- \to \tau^- \overline{\nu}_\tau$ Analysis

A new upper limit of $B^- \to \tau^- \overline{\nu}_\tau$ has been determined to be

$$\mathcal{B}(B^- \to \tau^- \overline{\nu}_\tau) < 5.7 \times 10^{-4} \text{ at } 90\% \text{ CL} \tag{7.4}$$

This is a significant improvement on the old value of 1.8×10^{-3} [14]. The new value sets a limit on the Type II Higgs sector parameter $\tan\beta/M_{H^\pm}$

$$\frac{\tan\beta}{M_{H^\pm}} < 0.38 \text{ GeV}^{-1} \text{ at } 90\% \text{ CL} \tag{7.5}$$

Appendix A

Fitting Procedure

A.1 General principles

The maximum likelihood method is employed to determine the upper limit of the $B^- \to \tau^- \overline{\nu}_\tau$ branching ratio. It is only applicable if the theoretical distribution from which the sample is taken is known. For most measurements in physics, this is either the Gaussian or Poisson distribution.

Suppose the parameter to be determined is μ, and the probability density function is $P(n|\mu)$, where n is the number of events. The method then consists of calculating the likelihood function

$$\mathcal{L} = \prod_i P_i(n_i|\mu_i) \tag{A.1}$$

where the product is taken over the i bins of the observed distribution. The principle now states that this function is a maximum for the true value of μ_i.

The parameter searched for in the analysis is the number of $B^- \to \tau^- \overline{\nu}_\tau$ decays. Thus μ_i in equation A.1 is

$$\mu_i = \mu_i^s + \mu_i^b \tag{A.2}$$

where μ_i^s id the Monte Carlo expected signal for a certain branching ratio of $B^- \to \tau^- \overline{\nu}_\tau$, and μ_i^b is the Monte Carlo predicted background. It is the parameter μ_i^s that is varied in determining the maximum of the likelihood function.

Poisson distributions are used when the number of events is very small, as is

the case in the $B^- \to \tau^- \overline{\nu}_\tau$ analysis. Then the likelihood function takes the form

$$\mathcal{L} = \prod_{\mathrm{i}} \frac{\mathrm{e}^{\left(-\mu_{\mathrm{i}}^{\mathrm{s}}+\mu_{\mathrm{i}}^{\mathrm{b}}\right)}\left(\mu_{\mathrm{i}}^{\mathrm{s}}+\mu_{\mathrm{i}}^{\mathrm{b}}\right)^{\mathrm{n_i}}}{\mathrm{n_i}!} \tag{A.3}$$

The product is over all the bins in both the leptonic and hadronic channel.

When upper limit determination is involved, then the procedure involves varying μ_i^s until 90% of the total area of the likelihood distribution is covered.

A.2 Fitting with limited Monte Carlo statistics

The Monte Carlo sample for this analysis is in fact about two times larger than the data sample, so fluctuations in the signal and background distributions are not negligible, rendering the number of expected signal(μ_i^s) and background(μ_i^b) Monte Carlo events unknown. The above procedure is modified to take this into account.

The probability to observe n_i data events in the i'th bin given the unknown underlying mean μ_i is,

$$P_i\left(n_i|\mu_i\right) = \frac{e^{-\mu_i}{\mu_i}^{n_i}}{n_i!} \tag{A.4}$$

The probability to have a given μ_i is constrained by the observed number of $B^- \to \tau^- \overline{\nu}_\tau$ (n_i^s) and background (n_i^b) events in the Monte Carlo:

$$P_i\left(\mu_i = \mu_i^s + \mu_i^b\right) d\mu_i = \frac{e^{-\mu_i^s}{\mu_i^s}^{n_i^s}}{n_i^s!}\frac{e^{-\mu_i^b}{\mu_i^b}^{n_i^b}}{n_i^b!} d\mu_i^s d\mu_i^b \tag{A.5}$$

The probability to observe n_i events is then expressed in terms of n_i^s and n_i^b by integrating over the unknown means μ_i^s and μ_i^b:

$$P_i\left(n_i|n_i^s, n_i^b\right) = \int\int P_i\left(n_i|\mu_i\right)\frac{e^{-\mu_i^s}{\mu_i^s}^{n_i^s}}{n_i^s!}\frac{e^{-\mu_i^b}{\mu_i^b}^{n_i^b}}{n_i^b!} d\mu_i^s d\mu_i^b \tag{A.6}$$

The integration can be performed analytically, and the result is given in reference [39]. The upper limit is determined by varying n_i^s in the likelihood function $\mathcal{L} = \prod_{\mathrm{i=1}}^{\mathrm{N}} \mathrm{P_i}\left(\mathrm{n_i}|\mathrm{n_i^s}, \mathrm{n_i^b}\right)$.

Bibliography

[1] M. Gell-Mann, Acta Physica Austriaca, **Suppl. IX** (1972) 733.

[2] S.L. Glashow, Nucl.Phys. **22** (1961) 579;
S. Weinberg, Phys.Rev.Lett. **19** (1967) 1264.

[3] C. Peterson *et al.*, Phys.Rev. **D27** (1983) 105.

[4] F.J. Gilman, M.B. Wise, Phys.Rev. **D27** (1983) 1128.

[5] T.A. DeGrand, R.D. Loft, Phys.Rev. **D38** (1988) 954.

[6] J.G. Bian, T. Huang Mod.Phys.Lett **8** (1993) 635.

[7] H. Krasemann Phys.Lett. **B96** (1980) 397.

[8] I. Claudio et. al., Phys.Rev. **D41** (1990) 1522.

[9] S.Aoki *et al.*, WA75 Collaboration, Prog.Theor.Phys.**89** (1993) 131.

[10] D.Acosta *et al.*, CLEO Collaboration, Phys.Rev. **D49** (1994) 5690;
D.Gibaut *et al.*, CLEO note CONF 95-22, June 1995.

[11] K.Kodama *et al.*, E653 Collaboration, preprint DPNU-96-33, June 1996.

[12] J.Z.Bai *et al.*, BES Collaboration, Phys.Rev.Lett **74** (1995) 4599.

[13] J.Richman and P.Burchat, Rev.Mod.Phys. **67** (1995) 893.

[14] D. Buskulic *et al.*, ALEPH Collaboration, Phys.Lett. **B343** (1995) 444.

[15] M.Artuso *et al.*, CLEO Collaboration, Phys.Rev.Lett. **75** (1995) 785.

[16] W.S.Hou, Phys.Rev. **D48** (1993) 2342.

[17] L3 Collaboration, B.Adeva *et al.*, Nucl.Instr.Meth. **A289** (1990) 35;
J.A.Bakken *et al.*, Nucl.Instr.Meth. **A275** (1989) 81;
O.Adriani *et al.*, Nucl.Instr.Meth. **A302** (1991) 53;
K.Deiters *et al.*, Nucl.Instr.Meth. **A323** (1992) 162;
B.Acciari *et al.*, Nucl.Instr.Meth. **A351** (1994) 300.

[18] R. Sumner *et al.*, Nucl.Inst.Meth. **A265** (1988) 252.

[19] H. Anderhaub *et al.*, Nucl.Inst.Meth. **A235** (1985) 267.

[20] M. Acciarri *et al.*, Nucl.Inst.Meth. **A351** (1994) 300.

[21] L3 Collab., Z.Phys. **C51** (1991) 179.

[22] T.Sjöstrand and M.Bengtsson, Comp.Phys.Comm **43** (1987) 367;
T.Sjöstrand, CERN preprint, CERN-TH.6488/92.

[23] R. Brun *et al.*, preprint CERN DD/EE/84-1 (Revised 1987).

[24] H.Fesefeldt, RWTH Aachen Report PITHA 85/02 (1985).

[25] L3 Collaboration, M.Acciari *et al.*, Phys.Lett. **B341** (1994) 245;
M.Acciari *et al.*, Phys.Lett. **B352** (1995) 487.

[26] R.M.Barnett *et al.*, Particle Data Group Phys.Rev. **D54** (1996) 1.

[27] J.Gronberg *et al.*, CLEO Collaboration, Phys.Rev.Lett. **75** (1995) 3232.

[28] W.Y. Chen *et al.*, CLEO Collaboration, Phys.Lett. **B226** (1989) 192.

[29] H. Albrecht *et al.*, ARGUS Collaboration, Z.Phys. **C53** (1992) 361.

[30] D. Buskulic *et al.*, ALEPH Collaboration, Z.Phys. **C69** (1996) 585.

[31] G.Alexander *et al.*, OPAL Collaboration, preprint CERN-PPE/96-51, April 1996.

[32] D.Buskulic *et al.*, ALEPH Collaboration, Z.Phys. **C62** (1994) 1;
P.Abreu *et al.*, DELPHI Collaboration, Z.Phys. **C59** (1993) 533;
G.Alexander *et al.*, OPAL Collaboration, Z.Phys. **C67** (1995) 27.

[33] Y. Pei, Z.Phys. **C72** (1996) 39.

[34] The LEP Experiments: ALEPH, DELPHI, L3, OPAL, *Electroweak Measurements and Constraints on the Standard Model*, preprint CERN-PPE/95-172.

[35] The L3 Collaboration, B* *Production in Z decays at LEP*, preprint CERN-PPE/94-143.

[36] J.Alexander *et al.*, CLEO Collaboration, contribution to the 28th International Conference on High Energy Physics, ICHEP-96, PA05-081.

[37] J. Hisano, H. Murayama and T. Yanagida, Nucl.Phys. **B402** (1993) 46.

[38] M.S.Alam *et al.*, CLEO Collaboration, Phys.Rev.Lett. **74** (1995) 2885.

[39] O. Adriani et. al., L3 Note 1637 (1994).

Vita

Tome Antičić was born on September 4th, 1969, in Split, Croatia. His education till entering University included schools in Germany, Croatia and Sudan. He completed his Bachelor of Science degree in 1990 at Queen Mary and Westfield College, University of London, after which he did the Part III of the Mathematics Tripos at Cambridge University. He enrolled in the graduate program of the Johns Hopkins University in Baltimore on September 1992 under Professor Peter Fisher. In 1995 he moved to Geneva, Switzerland to complete his graduate work at the L3 experiment at LEP. In April 1997 he completed his Doctor of Philosophy degree under Professor Chih-Yung Chien.